

Detection and Localization of Power and Coherence
Dynamics with EEG

DETECTION AND LOCALIZATION OF POWER AND
COHERENCE DYNAMICS WITH EEG

BY

AYDA GHAHREMANI, B.Sc.

A THESIS

SUBMITTED TO THE DEPARTMENT OF ELECTRICAL & COMPUTER ENGINEERING

AND THE SCHOOL OF GRADUATE STUDIES

OF MCMASTER UNIVERSITY

IN PARTIAL FULFILMENT OF THE REQUIREMENTS

FOR THE DEGREE OF

MASTER OF APPLIED SCIENCE

© Copyright by Ayda Ghahremani, December 2012

All Rights Reserved

Master of Applied Science (2012)
(Electrical & Computer Engineering)

McMaster University
Hamilton, Ontario, Canada

TITLE: Detection and Localization of Power and Coherence Dy-
namics with EEG

AUTHOR: Ayda Ghahremani
B.Sc., (Electrical Engineering)

SUPERVISOR: Prof. Kon Max Wong

NUMBER OF PAGES: x, 82

Detection and Localization of Power and Coherence
Dynamics with EEG

Ayda Ghahremani

December 14, 2012

Dedicated to all humans living in this world

Abstract

It has been observed by researchers that periodic auditory stimuli can cause the activities in different brain areas to be periodically synchronized. Fast auditory stimuli have been shown to cause the brain sources to synchronize at the rate of stimuli. Brain sources respond to them not only by increase in local synchronization, but also in the global synchronization of cortical regions often regarded as functional connectivity. Spectral power and coherence are often used to characterize such neural synchronization. Beta band oscillations have been reported to underlie the neural mechanism during repetitive auditory stimuli. Cortical generators of these underlying beta oscillations were investigated in several studies based on MEG measurements. This research is intended to investigate (1) EEG can be used to detect and localize neural sources changing in power and coherence and (2) beta oscillations underlie such neural synchronization during fast repetitive auditory stimuli based on EEG measurements. The procedure of this study consists of several steps. First, the minimum variance (MV) scalar beamformer, an adaptive spatial filter, is used to estimate the temporal signals in the brain source space, given EEG recordings. The analysis of the estimated source temporal signals then consists of two stages firstly the power analysis and secondly the coherence analysis. The dynamics of power and coherence is investigated instantaneously over time and in the lower beta frequency band

[14,20Hz]. This is done by detecting the most prominent changes in the two spectral parameters through singular value decomposition (SVD). Two coherence measures imaginary component (IC) and magnitude-squared coherence (MSC) are employed and compared in terms of their performance both mathematically and experimentally. In the simulations, we show the capability of using EEG to detect and localize power co-variations and dynamic functional connectivity in the cortical regions. We also perform the procedure on the recorded real data from subjects passively listening to rhythmic auditory stimuli. Beta oscillations are found to underlie the neural activity to percept auditory stimuli. This is shown by localization of auditory cortices and detection of power co-variation in this frequency band. We demonstrate the feasibility of using EEG to identify coupled and co-activated brain sources similar to those obtained from MEG signals in the previous studies. These include auditory and motor regions which were found to be functionally coherent and have a functional role in the auditory perception. The superiority of IC over MSC measure is proven mathematically and validated in both simulations and real data experiments.

Acknowledgements

First of all, I would like to thank my supervisor Dr K.M.Wong for his consistent supervision and patience during my research. He always encouraged me to make progress in my work. Also, I would like to express my sincere gratitude for his lessons of writing which I never forget in my life. Also, I am so grateful to Dr Aleksandar Jeremic for his advice and encouragement in the steps of my research.

Furthermore, I am so thankful of Dr Laurel Trainer in Department of Psychology, Neuroscience and Behaviour, McMaster University for providing me with the real EEG data and also for her great advices during data analysis. In addition, I am so grateful of Dr Dan Bosnyak in the same department to help me with the real data and in the preprocessing steps.

Also, I am so grateful to Department of Electrical and Computer Engineering, McMaster University for providing the academic environment to do research peacefully and become familiar with outstanding professors. Also, I am so thankful of Ms. Cheryl Gies for her administration and assistance.

Finally, I am so thankful of my husband and my family for their love and support.

Contents

Abstract	ii
Acknowledgements	iv
1 Introduction	1
1.1 Functional Interactions in the Brain	1
1.2 Spatial Filtering	4
1.3 Power Spectral Density	5
1.4 Coherence	6
1.5 Dynamical Interactions	7
1.6 Main Features of the Thesis	9
2 Preprocessing and Spatial Filtering	11
2.1 Preprocessing of EEG Signals	12
2.2 Head Model	13
2.3 Spatial Filtering	18
2.3.1 Model Definitions	18
2.3.2 Adaptive Spatial Filter	19
2.3.3 Determination of Source Orientation	23

2.3.4	Covariance Matrix	24
3	Instantaneous Power and Coherence	26
3.1	Extraction of Spectral Parameters	27
3.2	Instantaneous Power	29
3.3	Coherence	31
3.3.1	Elimination of Common Source Coherence Effect	33
3.4	Localization of Network	37
4	Implementation	40
4.1	Simulation	41
4.1.1	Comparison of Coherence Measures	41
4.1.2	Head Model and Spatial Filtering	44
4.1.3	Effect of Correlated Sources	45
4.1.4	Analysis of Performance	46
4.1.5	Detection and Localization of Power Response to Repetitive Stimulation	49
4.1.6	Detection and Localization of Coherency Response to Repeti- tive Stimulation	53
4.2	Real EEG Data	56
4.2.1	Procedure of Experiment and Preprocessing	61
4.2.2	Power Analysis	62
4.2.3	Coherence based Network	63
5	Summary,Future Work, and Conclusion	72
5.1	Summary and Conclusion of Thesis	72

5.1.1 Main Aspects of Research and Future Work 74

List of Figures

2.1	EEG recording components.	14
2.2	Triangulated surface of head (left) and cortex (right) taken from brainstorm (http://neuroimage.usc.edu/brainstorm) for boundary element method.	17
4.1	Instantaneous measure of coherence by MSC (blue) and IC (red). Bottom is the instantaneous SIR of the two signals (see text for more details).	43
4.2	Dependency of MSC on SIR when two signals are entirely zero phase-locked.	44
4.3	Talairach coordinate system, three main components of it are AC, PC and the vertical midsagittal plane. The image is from Center for Information Technology (CIT) (http://mipav.cit.nih.gov).	47
4.4	(a) Original waveform of the right auditory source. (b,c,d) the reconstructed waveform by different estimated covariance matrices. Covariance matrix is computed (b) at the snapshot when the sources are correlated, (c) uncorrelated, (d) over the whole period. Left column: correlation due to zero phase-locked coherency, and right column: correlation due to nonzero phase-locked coherency.	48

4.5	Results of the localized sources obtained by power estimation and the subsequent singular value decomposition in two different configurations. Two views of MRI, coronal (view from back) and sagittal (view from side), are displayed.	51
4.6	Effect of SNR on the reconstructed mixed configuration of superficial and deep sources in power analysis. (a) Upper : true source locations shown by yellow spots and source distribution for Middle : SNR = 5dB , and below: SNR = -5dB (the same MRI views as Figure 4.5 displayed).(b,c) Dominant temporal pattern of estimated power (solid, red curve) when (b) SNR = 5dB (c) SNR = -5dB overlaid by true power pattern (dashed, black curve).	52
4.7	Continued on the next page.	57
4.7	Source distribution corresponding to the first principal component obtained by IC and MSC metrics. In each subfigure, left: corresponding MSC and right: corresponding IC. (a): True distribution (reference source shown by a white solid circle and the coherent source by a cross hair), (b,c): Reconstructed source distribution for SNR = 15 and the varying regularization constant, (d,e): Reconstructed source distribution for SNR = 5 and also the varying regularization constant. Colorbar shows the intensity of the first principal component coefficients. The same MRI views as Figure 4.5 are displayed.	58
4.8	The first principal coherence waveform of the source distributions shown in Figure 4.7.	59

4.9	The temporal pattern of the first principal component of power fluctuations obtained from the phase-locked activity of brain sources. Overlaid power patterns of three subjects in A:390ms , B:585ms, and C:780ms conditions.	64
4.10	The source distribution corresponding to temporal patterns shown in Fig.4.9, averaged over subjects and projected onto the standard brain (sagittal and coronal views). Results are normalized and shown for the three conditions.	65
4.11	The first principal temporal coherence with left auditory source, shown for three individual subjects for A:390ms , B:585ms, and C:780ms conditions. Right column contains IC results and Left column contains MSC results.	69
4.12	Source distribution corresponding to the first principal component normalized to be in the range from 0 to 1 as shown in a color bar. Source distribution belongs to one of the subjects.	70
4.13	Normalized average of source distribution (absolute values) corresponding to the first principal component. The average is made over all subjects and conditions.	71

Chapter 1

Introduction

1.1 Functional Interactions in the Brain

Local specialization of brain sources and long-range cortical and subcortical functional interactions are necessary to study higher brain functions. Recent research studies have focused more on task-related functional network [12], [38] instead of only localizing activated, local brain areas. To study long-range functional interactions, neurophysiological data are needed which can be obtained by recordings from different parts of brain. These recordings can be Magnetoencephalography (MEG) or Electroencephalography (EEG). They have higher temporal resolution to track neural responses in comparison to other techniques such as Functional MRI. However, they lack spatial resolution to accurately identify task-related activity of anatomical regions in contrast to fMRI which has higher spatial resolution. Moreover, in order to study task-related neural responses millisecond temporal scale is of necessity making the analysis of EEG/MEG signals crucial.

Statistical interdependency of neurophysiological signals, characterized by functional connectivity, should be assessed to localize correlated long-range network. Functional connectivity has been observed in some studies with MEG and EEG [13, 39, 44]. Commonly, functional connectivity is defined in a specified frequency band. Coherent activity has been found among primary sensorimotor area (SM1), premotor cortex (PMC), supplementary motor area (SMA), and primary auditory cortex (A1) during auditory-guided paced movements [32] in alpha frequency band (8-12 Hz).

MEG has higher spatial resolution than EEG but, unlike EEG, is less distorted by conduction through the scalp and the skull. However, EEG is more easily available, more economical, and also sensitive to both tangential and radial sources (whereas MEG is not sensitive to radial sources). In a study with EEG [39], periodic power covariation of induced beta oscillations at the rate of auditory stimuli was observed in fronto-central surface channels. On the other hand, studies [13, 44] using surface channel responses of EEG to investigate functional connectivity and power changes during repetitive movement task have also been carried out. Identification of coherent network with EEG was performed in a very recent study with integration of auditory and visual stimuli in beta band (20 Hz) and gamma band (80 Hz) [20]. Fronto-parieto-occipital network and centro-temporal network were found in the mentioned frequency bands, respectively. In addition, localization of primary hand motor area and primary visual cortex was performed with a measure of functional connectivity based on EEG measurements [17].

Our hypothesis is that a stimulus may cause a coherent cortical and subcortical network to form and interact with each other following the stimulus. This interaction may be dynamic and in a periodic manner synchronized with periodic stimulus. The

interaction may also predict the timing of next stimulus by responding earlier than the next stimulus. In a recent MEG study [12, 39], dynamic interaction in fast auditory stimuli rate could predict the next stimulus. Dynamic cortico-cortical functional interaction with other stimuli have also been localized in both auditory and motor-related areas in beta band frequency (20 Hz) when subjects were listening to repetitive tone in a fast rate (1-3 Hz) without any movement. It has been suggested that beta oscillations are the signals for communications in auditory-motor networks. (Beta power reaches its maximum at the time of the stimuli and decreases immediately after.) This dynamic change has not yet been localized with EEG. In this study, we analyze neurophysiological data from all over the scalp with EEG recordings and localize their activity if they have dynamic interactions during fast rate stimuli. The methods are also implemented on real EEG data when subjects are listening to fast repetitive tones.

Localization of functionally connected network with EEG studies can be performed in either sensor space [13, 39, 44] or source space [17]. Field spread interference is a major obstacle to interpret functional coupling among sensor pairs and to attribute them to underlying brain sources. Spatial filtering is often performed to obtain source time signals [17, 38, 7] when dealing with EEG or even MEG scalp measurements. After extracting source time signals, a measure of identifying functional connectivity is of necessity. Power and coherence are two useful statistical measures which characterize how strongly a source is activated and how strongly sources are phase-locked in response to stimuli, respectively. Brain sources may show a synchronized response to stimuli by increasing in power or becoming phase-locked with other sources. Therefore, the two mentioned measures are helpful and complementary.

1.2 Spatial Filtering

Inverse algorithms can be used to map sensor measurements onto brain and can be divided into two categories – discrete dipole analysis [33] and source imaging [9, 29, 45]. In discrete dipole analysis, the number of sources needs to be known in advance. In source imaging, there is no need to know the number of sources. Therefore, we use source imaging in this research and refer to it with a general term "spatial filtering". Two classes of spatial filters used to map sensor data (here, EEG) onto brain sources are adaptive or non-adaptive filters. A non-adaptive filter is defined as a filter whose weights are computed independent of measurements. Weight-normalized minimum-norm method [9] and standardized low-resolution electromagnetic tomography (sLORETA)[29] are among the mostly used non-adaptive filters. In contrast, adaptive spatial filters depend on measurements. The most famous adaptive filter is Minimum Variance (MV) Beamformer. Weights of this filter are chosen so as to maximize brain electrical signal from a specified location (in a region of interest) while attenuating signals from other sources. The region of interest might be obtained from structural MRI of the subjects. It is firstly segmented into grey and white matter. Grey matter which is the most probable region for existence of source is then discretized. Afterwards, we compute weight vector for all predefined vertices. Finally, a three-dimensional image of source is reconstructed and local maxima in the image is considered to be the real source.

A comparison between MV beamformer and sLORETA have been carried out in [37]. The comparison was made between the localization ability of sLORETA and MV beamformer and showed sLORETA source reconstruction was more sensitive to Signal-to-Noise ratio (SNR), while normalized MV beamformer had no localization

bias even in the presence of noise. In addition, MV beamformer has higher spatial resolution than sLORETA. In this research, we have used MV scalar beamformer to extract source time signals. We will discuss the aspects of beamforming in greater details in Chapter 2.

1.3 Power Spectral Density

Power Spectral density is often used in the context of event-related synchronization (ERS) or event-related desynchronization (ERD). ERD/ERS represent frequency specific increase or decrease of power, respectively, which might reflect increase or decrease of synchronism among underlying neural populations. It is said to be complementary for Evoked Potential (EP) which is obtained by simple averaging (phase-locked response), because it is useful when the events are not necessarily phase-locked, but time-locked to the stimuli. ERD/ERS is often assessed with respect to a baseline or reference, usually defined in the time interval before applying a stimulus [31]. As an example, ERD was observed in the sensorimotor areas at 10 Hz and 20 Hz following a ERS during self-paced movements [23] with respect to a predefined baseline. In the cases where the events turn out to be predictable, it is difficult to define an appropriate baseline. For instance, in a study on the response to fast repetitive auditory stimuli, average of fronto-central sensor instantaneous power (in gamma band frequency) showed peak around the time of stimuli and in some subjects the same peak happened in a predictive manner sooner than the time of next stimuli [39]. Similar results were found in more details about the origins in a counterpart MEG study [12]. In this study, spatial filtering was employed to estimate source time series in the first steps and then, analysis of dynamics of brain sources' power was

done in the next steps. In the mentioned studies, it is a difficult or maybe impossible task to assign a baseline period. The reason is the fast periodic nature of stimuli which may cause the power of some brain sources dynamically oscillates in the same frequency as stimuli and might predict the next stimuli. In this case, ERD/ERS may not be exactly time-locked to the stimuli. Therefore, we might expect the peak of power occurring at any time between the stimuli. In Chapter 3, a method is proposed to localize sources whose power dynamics co-varies and is synchronized with stimuli, without determining a baseline period.

1.4 Coherence

Coherence is the second and complementary measure besides power spectral density to study functional connectivity in the brain. It is often used to study long-range coherence in brain cortical network in higher brain functions. Coherence shows how consistent is the phase and magnitude relation between two neural signals. In other words, it quantifies the statistical dependency between the two neural time series. Generally, coherency is a complex-valued quantity and often magnitude-square of coherency called magnitude-squared coherence (MSC) is alternatively regarded as the measure of coherence. Coherence has been used to study functional connectivity from scalp sensor measurements [44, 26, 40]. [44] has examined the effect of movement rate on the functional connectivity of cortical motor areas. The problem with sensor-based coherence analysis is that we cannot infer underlying source functional connectivity because of volume conduction. Some solutions have been proposed by [26, 40]. [26] proposed to use the imaginary component (IC) which eliminates interference due to spatial spread of source activity on the scalp by canceling zero-phase lag coherence.

[40] used surface Laplacian alternative to direct sensor measurements. Although these methods have proved to be helpful, still they do not give information about the underlying sources. More appropriate strategy is to project the sensor data onto the brain and do coherence analysis in source domain and has been used in several papers [12, 32, 30]. As power spectral density, coherence is also defined for a specific frequency range.

As discussed above, to analyze brain functional connectivity, application of spatial filtering is of necessity to estimate source time signals of brain, thereafter coherence is subsequently computed among the pairs. The common problem of spatial filtering, is the spatial leakage of the inverse algorithm. This leakage often causes spurious coherence in the reconstructed source image. In this thesis, this effect is called common source effect. Some solutions have been proposed to avoid this problem including use of IC [38] or use of lagged component [30] instead of MSC. These two measures eliminate zero-phase coherence which comes from a common source between two neural sources. In this thesis, we use the imaginary component to localize the coherent network among the sources, as explained in Chapter 3.

1.5 Dynamical Interactions

Two measures have already been proposed , power spectral density and coherence , to examine frequency-specific ERS/ERD (Local interactions) and long-range functional connectivity (global interactions), respectively. Dynamic changes of power and coherence have been characterized in several studies and have been shown to play an important role in temporal prediction during fast periodic auditory stimuli [12, 32, 39]. In this study, we use these measures to localize two kinds of neural network in the

brain. The first one which is called power-based network (POW-NET) is based on co-variation of power. In other words, this network contains sources which synchronize and desynchronize simultaneously when periodic stimuli is applied, as shown in [12]. The second network is called coherence-based network (COH-NET): Given a reference source, COH-NET consists of sources which become functionally connected or disconnected at the same time with the reference source during periodic stimuli. As described earlier, in the fast periodic stimulation it is a difficult or impossible task to determine a constant baseline period to contrast with post stimuli neural activity. The reason is the ERS/ERD and functional connectivity have temporal dynamic pattern in this situation [12] and state of some sources might change at any time before stimuli (prediction) or any time even after stimuli [12, 39]. Particularly, it was shown in a study with MEG that POW-NET included some regions of motor, frontal and auditory cortices and some subcortical regions such as cerebellum and thalamus. COH-NET included several frontal and temporal cortices given a reference source in motor cortex. In this study, we show the feasibility of obtaining similar results during fast auditory stimuli through proper EEG analysis. The proposed coherence measure is IC. In Chapter 3, we show the advantage of using this measure over MSC used in [12] to eliminate spurious coherence. The reference source for coherence estimation is specified based on a priori knowledge. Firstly, we compute the instantaneous power of all source time series itself and instantaneous coherence of all sources based on a reference source. Then, we use Singular Value Decomposition (SVD) to detect the principal temporal pattern in power and coherence during stimuli. A criterion is proposed to maintain significant sources. Sources which have the same temporal pattern

of power are included in POW-NET and those which have the same temporal pattern of coherence with the reference source is considered as COH-NET. Simulations are also performed to show the efficacy of method with synthetic data. In computer simulations, several sources mimic the activity of POW and some other sources are functionally connected and phase-locked with POW sources thereby making COH group. The accuracy of the algorithm is then assessed. The two coherence measures IC and MSC are also compared.

1.6 Main Features of the Thesis

- Preprocessing of EEG signals including artifact rejection, band pass filtering, are firstly explained. Appropriate head model is chosen to construct a forward model. This is a necessary step before spatial filtering. MV scalar beamformer is mathematically derived and its different aspects are discussed (Chapter 2).
- To do source space feature extraction, Hilbert transform is used to obtain the analytic signals, followed by the estimation of power and coherence. The variation of two coherence measures IC (proposed) and MSC with respect to SNR of sources are compared. SVD is employed to obtain the principal temporal pattern in power and coherence and subsequently localize them. POW-NET and COH-NET were localized based on the sources having common temporal pattern of power and coherence, respectively. An error-based criterion is used as threshold for localization.
- In the simulations section, we show the performance of the proposed algorithm to find POW-NET and COH-NET. The applicability of the method is shown on

real data and confirms the feasibility of using EEG to track dynamic interaction of sources.

Chapter 2

Preprocessing and Spatial Filtering

Electroencephalogram (EEG) signals provide an indirect measurement of neural activity in the brain. In this chapter, we explain the procedure to estimate neural signals of brain, given EEG scalp measurements. The necessary step prior to every analysis with EEG is preprocessing and artifact rejection. First, the durations of signals consisting of the response to one or several stimuli are segmented. Channels showing unusual behavior should be recognized and a proper strategy should be applied. The recorded EEG signals are mostly contaminated by muscle and eye blink artifacts. The periods contaminated by these artifacts have to be removed. The remaining epochs of EEG data should then be band-pass filtered in the frequency band of interest, which, in our case, is the lower beta frequency band [14, 20Hz].

In general, source localization consists of solving two kinds of problems: 1- the forward problem 2- the inverse problem. The forward problem is to determine the potential distribution on the scalp due to different source configurations in the brain. The inverse problem is to estimate source position and characteristics given scalp potential distribution. Therefore, source space reconstruction consists of two steps:

1- choosing an appropriate head model to build a forward model 2- given the scalp measurements and a head model, spatial filtering is performed to estimate brain source time series. In this chapter, we explain this procedure in great details.

2.1 Preprocessing of EEG Signals

Figure 2.1 shows the typical components of EEG recording system. At the first step, the scalp signals due to current sources shown by arrows are passed through a differential amplifier. A low-pass analog filter is usually applied to keep the most of signal power in the range of frequency less than 100 Hz. In addition, a high-pass filter may also be used to eliminate the substantial power below 0.5 Hz. A notch filter may or may not be used to remove power line frequency component (50 or 60 Hz). The difference signal is then boosted with a certain gain and passed through an analog to digital convertor (ADC). EEG data were then stored and further off-line analysis is performed on them including time-frequency analysis, spatial filtering, and etc. The difference signal consists of individual sensor signals and a reference sensor signal usually chosen to be far from active region. The choice of reference is important and may lead to wrong interpretation of the signals; the linked-ears or linked-mastoids is a popular reference used in most cognitive laboratories [27]. No matter which reference is to be chosen, EEG signals are better to be re-referenced to the average signal to diminish the reference signal influence [27].

In this research, both real and simulated EEG data were recorded based on Biosemi 128-channel system (BioSemi, Amsterdam, Netherlands). In this configuration, 128 closely spaced sensors are placed on the scalp. There are some stages of preprocessing on the average-referenced real EEG signals which should be taken

before the source analysis. Initially, channels showing unusual behavior should be eliminated from the further analysis. The common procedure is to omit these channels or to interpolate them based on all the other channels. The next step is to segment EEG signals which cover the response to one or several repetitive auditory stimuli. Then, segments including artifacts need to be rejected. The origin of these artifacts is mostly eye blink or muscle activities. There are different approaches to deal with these artifacts. Clinical experts use visual inspection to detect artifacts and replace the samples of artifacts. One may use the concept of outliers in the statistical data [28] and replace the artifacts with random samples having the same distribution with data. Since this is not the issue of this study, we do not explain the artifact rejection methods in great details. The method we have used for the real EEG data is based on the amplitude threshold [44, 39]; artifacts usually have greater amplitude in comparison to normal brain signals. In this manner, segments whose amplitude is greater than a certain threshold are not used for the further analysis.

2.2 Head Model

As described at the beginning of this chapter, forward problem is the problem of determining the potential distribution given any source configuration in the brain. To solve an inverse problem, forward model should be determined in advance. To perform forward modeling, a proper geometry and conductivity properties of different head tissues need to be determined. The inaccuracy of determining these characteristics can lead to the inaccuracy of forward model and subsequently mislocalization in the inverse model. The most common head model is the three-concentric sphere consisting of three layers brain, skull and scalp. In this model, the conductivity is

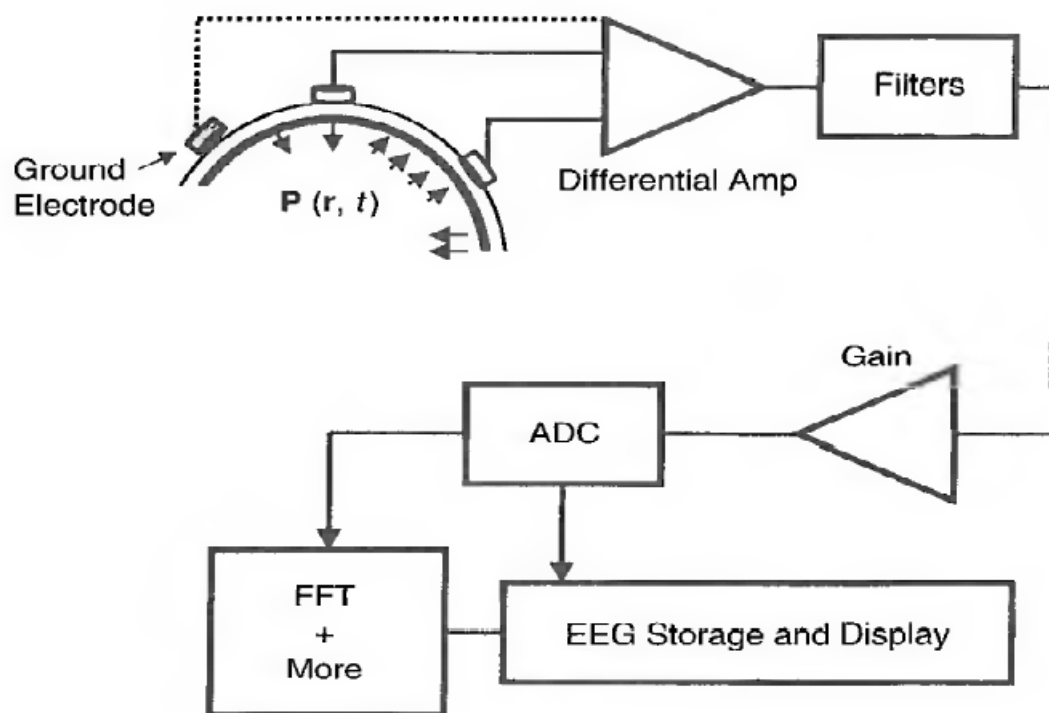


Figure 2.1: EEG recording components.

assumed to be homogeneous and isotropic in each layer. Given this spherical model, the forward model has a closed-form solution [25]. Since head is not a sphere in shape, realistic geometry of brain using MRI is often preferred to the spherical geometry. The procedure of scanning subjects for the structural MRI in every EEG experiment is becoming more common to obtain a more accurate geometry.

Given the realistic head geometry, the forward problem is solved using boundary element method (BEM) and finite element method (FEM) [41, 3]. To implement BEM, the boundary of tissues needs to be specified (skin, skull, cortex) which is obtained by segmentation of subject's anatomical MRI. The boundary surface is then triangulated in 3-D space (see Fig 2.2). BEM is often regarded as a semi-realistic piece-wise constant conductivity model. FEM is also based on the realistic geometry of head, but it can also handle anisotropic, inhomogeneous tissue which is the case for the bone tissue in the head model. To perform FEM, the discretization should be carried out over the whole volume of tissues. The advantage of BEM over FEM is its lower computational costs, because the unknowns of BEM are only in the interfaces while in FEM they are within the whole discretized volume. On the other hand, determination of anisotropic properties of the tissues is not a trivial task yet. In our study, we use boundary element model for the above reasons. Most boundary element methods suffer from accuracy issue, when the conductivity ratio between two neighboring tissues is high. [16] has suggested a new method called symmetric BEM to overcome this critical problem. We have used the software called OpenMEEG which implements this technique and was also built by [16].

In order to make a forward model with the boundary element method, we need a

realistic representation of the head geometry, electrode positions, conductivity properties of the tissues (assumed to be homogeneous and isotropic). To build an appropriate head model, we need to combine the anatomical information often obtained by structural MRI with EEG measurements. Since MRI and EEG are two different brain recording modalities defined in two separate coordinate systems, we need to express both data in the same coordinate system. Coordinate system of EEG measurements is often defined based on the anatomical landmarks outside of head, including nasion,inion, left pre-auricular (LPA) point and right pre-auricular (RPA) point¹, whereas the coordinate system used for MRI is defined based on the internal landmarks such as anterior and posterior commissure. We need to use a unified coordinate system and explain the coordinates of EEG sensors and structural MRI voxels in this coordinate system. The coordinate system we used in our study can be described as follows: x-axis goes from the origin (midway on the line connecting LPA to RPA) to the nasion, the y-axis goes from the origin through the LPA and intersects x-axis at a right angle and the z-axis goes upward and is orthogonal to the xy-plane.

Now, we summarize the whole strategy to prepare the forward model. A structural MRI with voxel size of $1 \times 1 \times 1 \text{mm}^3$ is transformed into the coordinate system defined above. Three landmarks the nasion and the left and right pre-auricular points are found and marked in the structural MRI. A rotation and shift of the 3D-volume is needed [11], so that all the 3-D points of MRI are expressed in the new coordinate system defined by the three landmarks. The structural MRI is then segmented and the outer layer of scalp and the inner and the outer layer of skull are extracted and discretized into sufficient number of vertices. Then, given each segment's conductivity,

¹These anatomical landmarks are located surrounding a head, for instance inion is a prominent point at the back of the head.

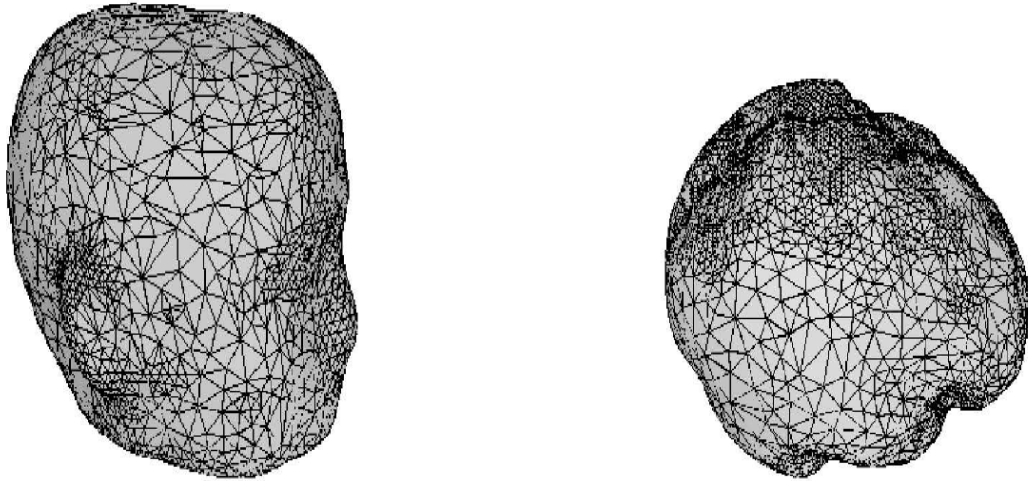


Figure 2.2: Triangulated surface of head (left) and cortex (right) taken from brainstorm (<http://neuroimage.usc.edu/brainstorm>) for boundary element method.

boundary element method is used to evaluate the potential distribution at given electrode coordinates. In this research, we have used a default MRI (Colin 27) for both simulations and real data. For the real data, 3D-coordinates of sensors were obtained before the EEG experiments. Since the individual subjects' MRI was not available, the individual electrode coordinates were projected onto the default MRI. The procedure was performed with Brainstorm software [42], which is documented and freely available for downloading online under the GNU general public license (<http://neuroimage.usc.edu/brainstorm>).

2.3 Spatial Filtering

2.3.1 Model Definitions

We denote the electric signal measured by M sensors at time t as a real vector $\mathbf{m}(t) = [m_1(t) \cdots m_M(t)]^T$. A source is defined by three parameters including spatial location, magnitude and orientation (the latter two determine the source moment). Spatial location of a source is given by a three dimensional vector $\mathbf{q} = [q_x \ q_y \ q_z]^T$. At time t and at location \mathbf{q} , the magnitude of the source is represented by a real quantity $s(\mathbf{q}, t)$ and its orientation is given by $\boldsymbol{\mu}(\mathbf{q}) = [\mu_x(\mathbf{q}) \ \mu_y(\mathbf{q}) \ \mu_z(\mathbf{q})]^T$ whose components are the cosine of angle between the source moment and three main axes, x, y, z . The *leadfield* vector $\mathbf{a}(\mathbf{q}, \boldsymbol{\mu})$ comprising of M elements from the sensors can be conceived as a combination of responses from unit sources at \mathbf{q} in the directions x, y, z so that it can be written as $\mathbf{a}(\mathbf{q}, \boldsymbol{\mu}) = [\mathbf{a}_x(\mathbf{q}) \ \mathbf{a}_y(\mathbf{q}) \ \mathbf{a}_z(\mathbf{q})]\boldsymbol{\mu}(\mathbf{q})$, where $\mathbf{a}_x(\mathbf{q}), \mathbf{a}_y(\mathbf{q}), \mathbf{a}_z(\mathbf{q})$ are respectively the unit response vectors in the three dimensions x, y, z . Often this unit-response matrix is written as $\mathbf{A} = [\mathbf{a}_x(\mathbf{q}) \ \mathbf{a}_y(\mathbf{q}) \ \mathbf{a}_z(\mathbf{q})]$ which is called the *leadfield matrix*.

By superposition law, we can compute sensor data given source moment $s(\mathbf{q}, t)$ at time t as below

$$\mathbf{m}(t) = \int \mathbf{a}(\mathbf{q}, \boldsymbol{\mu})s(\mathbf{q}, t)d\mathbf{q} \quad (2.1)$$

In a more realistic situation, measurement noise and errors due to modeling inaccuracy are taken into account by adding an extra term $\mathbf{n}(t)$ to the above model as additive noise. The signal model given by Eq.3.12 is often called the forward model. The components of $\mathbf{a}(\mathbf{q}, \boldsymbol{\mu})$ are constructed by BEM given the geometry of head, conductivity properties of head tissues, and sensor positions as described in previous

section. Given the sensor measurements $\mathbf{m}(t)$, and given the forward model, our first goal here is to recover the source moment. For this purpose, a linear spatial filter in the form of a weight vector $\mathbf{w}(\mathbf{q})$ is applied to achieve an estimate of $s(\mathbf{q}, t)$ such that

$$\hat{s}(\mathbf{q}, t) = \mathbf{w}^T(\mathbf{q})\mathbf{m}(t) \quad (2.2)$$

where $\hat{s}(\mathbf{q}, t)$ is the source magnitude (orientation is assumed to be known here) and $\mathbf{w}(\mathbf{q})$ is a weight vector to be evaluated, where $(\cdot)^T$ denotes the transpose sign.

2.3.2 Adaptive Spatial Filter

In order to estimate source magnitude, we employ an adaptive spatial filter called minimum variance (MV) scalar beamformer (also called SAM) [45]. Generally, this kind of spatial filtering aims to pass the corresponding source with unit gain and suppresses the interference of other sources. For a MV scalar beamformer, the weight vector $\mathbf{w}(\mathbf{q})$ is obtained for a source located at \mathbf{q} by finding the solution to

$$\min[\mathbf{w}(\mathbf{q})^T \mathbf{R}_m \mathbf{w}(\mathbf{q})] \quad (2.3)$$

subject to the following constraint

$$\mathbf{a}(\mathbf{q}, \boldsymbol{\mu})^T \mathbf{w}(\mathbf{q}) = 1 \quad (2.4)$$

where \mathbf{R}_m is the covariance matrix of the sensor measurements obtained by $\mathbf{R}_m = \langle (\mathbf{m}(t) - \bar{\mathbf{m}})(\mathbf{m}(t) - \bar{\mathbf{m}})^T \rangle$, where $\bar{\mathbf{m}}$ is the mean value of $\mathbf{m}(t)$ and $\langle \cdot \rangle$ denotes the ensemble average which maybe replaced by time average in practice or the average

over a number of trials. In our study, we obtain the average over several trials as well as over time samples so that the variability and independency of data are increased. We explain more about this in Section 4.1.3. Solution to Eq.2.3 can be found by the method of Lagrange multipliers, we define Lagrangian as below

$$\mathbf{L}(\mathbf{w}, \kappa) = \mathbf{w}^T \mathbf{R}_m \mathbf{w} + \kappa(\mathbf{w}^T \mathbf{a} - 1) \quad (2.5)$$

where κ is the Lagrange multiplier and \mathbf{a} and \mathbf{w} are real-valued quantities and \mathbf{R}_m is a positive-definite matrix. Therefore, Lagrangian is a real-valued quantity. The dependency of $\mathbf{a}(\mathbf{q}, \boldsymbol{\mu})$ to \mathbf{q} and $\boldsymbol{\mu}$ and the dependency of $\mathbf{w}(\mathbf{q})$ to \mathbf{q} were dropped for simplicity in the formulation. To minimize Lagrangian, we take the derivative of Lagrangian with respect to \mathbf{w} as below

$$\frac{d\mathbf{L}(\mathbf{w}, \kappa)}{d\mathbf{w}} = 2\mathbf{R}_m \mathbf{w} + \kappa \mathbf{a} \quad (2.6)$$

We set the right hand-side to zero, then \mathbf{w} is

$$\mathbf{w} = \frac{-\kappa \mathbf{R}_m^{-1} \mathbf{a}}{2} \quad (2.7)$$

We substitute \mathbf{w} in the constraint (Eq. 2.4) and obtain κ

$$\kappa = \frac{-2}{\mathbf{a}^T \mathbf{R}_m^{-1} \mathbf{a}} \quad (2.8)$$

the final solution can be written as below

$$\mathbf{w} = \frac{\mathbf{R}_m^{-1} \mathbf{a}}{\mathbf{a}^T \mathbf{R}_m^{-1} \mathbf{a}} \quad (2.9)$$

The constraint $[\mathbf{a}^T \mathbf{w} = 1]$ shows the fact that the norm of a weight vector depends on the norm of a leadfield vector. Because of electromagnetic properties, the leadfield vector depends on the location of the sources. Then, the closer is a source to the center of the head, the lower is the norm of its leadfield vector and the weight vector may go to a dramatic higher value and becomes unstable. For this fact, leadfield vector is often normalized by replacing \mathbf{a} with $\frac{\mathbf{a}}{\|\mathbf{a}\|}$. Unit-norm constraint on \mathbf{w} may also be useful to derive a stable weight vector. For example, another form of beamforming is called unit-noise gain minimum variance beamformer, the weight vector is obtained as below

$$\min[\mathbf{w}^T \mathbf{R}_m \mathbf{w}] \quad (2.10)$$

subject to the following constraints

$$\mathbf{a}^T \mathbf{w} = \tau$$

$$\mathbf{w}^T \mathbf{w} = 1$$

To find the solution to Eq. 2.10, we should firstly find the solution to the first constraint. Then, we obtain the value of τ by substituting the solution \mathbf{w} in the second constraint [34]. There is no need to normalize the leadfield vector in this case, because the norm of the weight vector is already constrained.

Although the weight vector is built to suppress the interference as much as possible, it has been shown that it cannot fully block the interference of perfectly correlated signals [35]. This may have influence on the reconstructed signal intensity or may cause distortion in the source signals which is called signal cancellation. One remedy

for this problem is the use of nulling constraints [21]. In the simple words, this problem can be handled by putting more constraints on the weight vector which blocks the interference caused by the correlated sources. Such spatial filtering is called linearly-constrained minimum-variance (LCMV) beamformer ; The weight vector is obtained by minimizing the output power and at the same time blocking the signals of other interfering sources

$$\min[\mathbf{w}(\mathbf{q})^T \mathbf{R}_m \mathbf{w}(\mathbf{q})] \quad (2.11)$$

subject to the following constraints

$$\begin{cases} \mathbf{a}(\mathbf{q})^T \mathbf{w}(\mathbf{q}) = 1 \\ \mathbf{a}(\mathbf{q}_1)^T \mathbf{w}(\mathbf{q}) = 0 \\ \vdots \\ \mathbf{a}(\mathbf{q}_n)^T \mathbf{w}(\mathbf{q}) = 0 \end{cases} \quad (2.12)$$

the weight vector is obtained by passing the source signal from a certain location \mathbf{q} with unit gain and imposing a null constraint on the other sources at locations $\mathbf{q}_1, \mathbf{q}_2, \dots, \mathbf{q}_n$. which are expected to be correlated with the source of interest. The final solution is then derived in [34] and is expressed as below

$$\mathbf{w} = \mathbf{R}_m^{-1} \mathbf{C} [\mathbf{C}^T \mathbf{R}_m^{-1} \mathbf{C}]^{-1} \begin{pmatrix} 1 \\ 0 \\ \vdots \\ 0 \end{pmatrix} \quad (2.13)$$

where \mathbf{C} is defined as $\mathbf{C} = [\mathbf{a}(\mathbf{q}) \quad \mathbf{a}(\mathbf{q}_1) \quad \dots \quad \mathbf{a}(\mathbf{q}_n)]$. As the location of correlated

sources should be known in order to use these constraints, it is not widely employed.

In this research, we use MV scalar beamformer as it is widely used and validated by [37, 5]. It will be shown in the simulations that the problem of partly correlated sources in time is solved by an appropriate choice of data to compute the covariance matrix. In this manner, if the covariance matrix is properly estimated, there is no signal cancellation in the reconstructed source time series.

The computation of $\mathbf{w}(\mathbf{q})$ in Eq.2.9 necessitates the knowledge of probable source position \mathbf{q} in the source space and the orientation parameter $\boldsymbol{\mu}(\mathbf{q})$. The source space is commonly constrained to the grey matter which is extracted from the individual anatomical MRI and the region is discretized into a number of grids (as described in Section 4.1.2). To determine the orientation, there are different methods to estimate orientation vector $\boldsymbol{\mu}(\mathbf{q})$ such as the ones in [17] and [36]. In the next section, we introduce the most important methods to determine orientation. The weight vector $\mathbf{w}(\mathbf{q})$ is computed by Eq.2.9 for all vertices in the sources space and the source waveforms are reconstructed.

2.3.3 Determination of Source Orientation

Several methods have been proposed to determine the source orientation [8, 36]. One simple method is to use anatomical constraints. Since EEG sources are primarily expected to be due to the apical dendrites of cortical pyramidal cells² and the cortex has a columnar organization³, the local source would be perpendicular to the cortical surface [8]. This is consistent with the results obtained by subdural and intracortical

²Pyramidal cells are a type of neuron distributed in the cerebral cortex, the hippocampus and the amygdala and the apical dendrites are a dendrite that branches from the apex of it.

³Cortical pyramidal cells are located in a column-wise manner.

recordings [1, 24]. In addition, There are several mathematical methods to obtain the optimum orientation of sources which are based on the MV scalar beamformer. One way is to maximize output power of spatial filtering [37]. Substitute the weight vector Eq 2.9 into Eq 3.11. Then, the power of source can be described as below

$$\langle \hat{s}^2(\mathbf{q}, t) \rangle = [\mathbf{a}^T \mathbf{R}_m^{-1} \mathbf{a}]^{-1} = [\boldsymbol{\mu}^T \mathbf{A}^T \mathbf{R}_m^{-1} \mathbf{A} \boldsymbol{\mu}]^{-1} \quad (2.14)$$

where $\boldsymbol{\mu}$ and \mathbf{A} are the orientation vector and the leadfield matrix at location \mathbf{q} , respectively (see Section 2.3.1 for more details). Then, we need to minimize $[\boldsymbol{\mu}^T \mathbf{A}^T \mathbf{R}_m^{-1} \mathbf{A} \boldsymbol{\mu}]$ in order to maximize the power expression. The minimum corresponds to the minimum eigenvalue of the matrix $\mathbf{A}^T \mathbf{R}_m^{-1} \mathbf{A}$ as shown in [36] and the $\boldsymbol{\mu}$ which minimizes the expression is the eigenvector corresponding to the minimum eigenvalue.

In this research, we assume that sources are perpendicular to the cortical surface as validated by [8]. We obtain the anatomical information about the orientation of the cortical surface after triangulation of it and use the information

2.3.4 Covariance Matrix

In the computation of $\mathbf{w}(\mathbf{q})$ in Eq. 2.9, additional consideration should be taken into the covariance matrix \mathbf{R}_m which may become unstable due to two reasons 1- insufficient number of trials and/or insufficient temporal data for averaging, 2- correlation among sources. The number of data for averaging needed to make the covariance matrix well-conditioned should be more than the number of electrodes [34]. There are several solutions proposed to deal with this problem. Diagonal loading is a common procedure and typical approach. The idea of diagonal loading is to increase the diagonals of covariance matrix by a pre-specified amount. This is done by replacing

\mathbf{R}_m^{-1} with $(\mathbf{R}_m + \alpha\mathbf{I})^{-1}$ where α is a regularization constant. Increasing α helps to improve signal-to-noise (SNR), but spatial specificity is decreased. The value of α is chosen to make a trade-off between SNR and the spatial resolution. A method called Bayesian Principal Component Analysis [46] has been proposed which gives an objective solution to make a trade-off between the stable covariance matrix and the spatial specificity. Beamspace processing [34] is another technique which reduces the dimensionality by including a priori knowledge about source locations and maybe their configurations.

In our study, we have used diagonal loading which is the most common approach. The appropriate amount of α is chosen experimentally relative to the maximum eigenvalue of the covariance matrix. Furthermore, we see in the simulations that the correlation among sources has a confounding effect on the reconstructed source waveforms. This problem is solved, if the covariance matrix is computed from EEG data over time besides trials.

Chapter 3

Instantaneous Power and Coherence

We have already explained the procedure to estimate the neural source time series based on the scalp EEG measurements. After the source time series are extracted, two kinds of stimulus-sensitive networks need to be characterized to localize and identify dynamical cortical interactions. Firstly, power-based networks (POW-NET) consist of sources whose power spectral density co-varies dynamically with stimuli. Secondly, coherence-based networks (COH-NET) consist of sources whose consistency of phase and amplitude relation (coherence) with a reference source co-changes dynamically with stimuli.

In order to localize these networks, we need to extract instantaneous amplitude and phase of sources based on their estimated time series at the very first stage. Then, instantaneous power spectral density and an instantaneous coherency measure are computed. The first quantity obtained for coherency is a complex number. Therefore, often magnitude-squared coherence (MSC) quantifies the amount of coherency. MSC

has been shown to give rise to spurious coherence caused by spatial leakage due to spatial filtering methods (also called zero-phase coherence). In this study, we will show that even subtraction by MSC's mean over time cannot cancel the zero-phase coherence in the low SNR situation. We propose an alternative coherence measure imaginary component (IC) to study dynamical changes of coherence which eliminates the zero-phase coherence even in the low SNR situation (see a mathematical comparison between the two measures in Section 3.3.1).

In the Section 3.4, two sets of data features already collected including the instantaneous power and the instantaneous coherence (MSC and IC) are decomposed into their principal components and the most significant locations are subsequently identified as the nodes of POW-NET and COH-NET. In addition, the associated dominant temporal pattern of power and coherence is also identified to track dynamical changes with stimuli.

3.1 Extraction of Spectral Parameters

In order to estimate power spectral density and coherence, we need to first achieve a spectro-temporal representation of the source signals which is a complex-valued quantity at a certain time and frequency. This is actually a two-dimensional representation of a signal in time-frequency domain. At time t and at frequency f , $\hat{z}(f, t)$ is the spectro-temporal representation of a source signal $\hat{s}(t)$ has phase $\hat{\phi}_z(f, t)$ and amplitude $\hat{a}_z(f, t)$ as below (here, we dropped the dependency on the location parameter \mathbf{q} from $\hat{s}(\mathbf{q}, t)$ for simplification in the notations)

$$\hat{z}(f, t) = \hat{a}_z(f, t)e^{i\hat{\phi}_z(f, t)} \quad (3.1)$$

there are several common methods to achieve the spectro-temporal representation of signals, including *Fourier*, *wavelet* and *Hilbert* approaches [4].

The Fourier-based analysis (called *short-time Fourier analysis*) uses a sliding window which usually has a certain window function (to avoid spectral leakage) with smooth flanks. Each segment of signal is then multiplied by this window function and the discrete Fourier transform is applied. The transform gives a complex-valued time-frequency representation of the signal. The actual time-frequency resolution solely depends on the length of the sliding window and to a lesser degree on the shape function of it. The wavelet analysis is another technique to find the spectro-temporal representation of the signal. In this analysis, the time-frequency representation is obtained by convolving the signal with a number of kernels, called *wavelets*. The temporal resolution depends on frequency dependant wavelet length.

The third technique is based on the Hilbert analysis. As in the Fourier analysis in which a signal was segmented in time and the Fourier spectrum was computed for each segment; in Hilbert approach, the signal is firstly transformed into neighboring frequency components via a bandpass filter. Then, the *analytic* signal for each component is computed which gives a spectro-temporal representation in different time and frequencies. [4] showed that these three techniques are "formally equivalent as long as the relevant analysis parameters are matched with each other". In this study, we use the Hilbert method to represent the spectro-temporal properties of the reconstructed source signals only in the lower beta frequency band from 14Hz to 20Hz shown in [12] to underlie neural interactions in response to repetitive auditory stimuli. Therefore, the signals are band-pass filtered in this frequency band of interest. In both real data and simulations, this is applied to EEG data prior to spatial filtering. In the next

step, the Hilbert transform is applied to the band-pass filtered signal $\hat{s}_b(t)$ as below (we replace f by b to emphasize the single lower beta frequency band considered in this research)

$$\hat{s}_{h,b}(t) = \frac{1}{\pi} \text{P.V.} \int_{-\infty}^{\infty} \frac{\hat{s}_b(t)}{t - \tau} d\tau \quad (3.2)$$

with P.V indicating the Cauchy principal values and $\hat{s}_{h,b}(t)$ is the Hilbert transform of $\hat{s}_b(t)$ which is band-pass filtered at the frequency band $[b - \Delta b, b + \Delta b]$ where b is the center frequency of the lower beta band. In the frequency domain, this is equivalent to

$$\hat{S}_{h,b}(\nu) = -j \text{sgn}(\nu) \cdot \hat{S}_b(\nu) \quad (3.3)$$

where $\hat{S}_b(\nu)$ is the Fourier transform of $\hat{s}_b(t)$ and $\text{sgn}(\cdot)$ denotes the sign function.

Then, the analytic signal (spectro-temporal representation) is written as below .

$$\hat{z}(b, t) = \hat{s}_b(t) + i\hat{s}_{h,b}(t) = \hat{a}_z(b, t)e^{i\hat{\phi}_z(b, t)} \quad (3.4)$$

The analytic signal of all the sources is computed subsequently in the same manner. Once the spectro-temporal representation of the signals are built, a variety of statistical measures such as power and coherence can be computed. From now on, we drop the dependency of the analytic signal and statistical measures to b , but we know that all the analysis is performed in the frequency band of interest.

3.2 Instantaneous Power

Power spectral density has been used for the analysis of event-related synchronization or desynchronization (ERS or ERD) of neurophysiological signals [31, 39]. ERS/ERD

commonly refers to increase/decrease of power spectral density of neural responses after a particular task which the subject repetitively performs or after an external stimuli is repetitively applied. It is often defined with respect to a predefined baseline power. Often, ERS/ERD is represented for a specific frequency and the importance of studying ERS/ERD lies in the fact that ERS/ERD of a neurophysiological signal recorded from a cortical region reflects the increase or suppression in the neural synchrony. This phenomenon has been observed in EEG and MEG measurements which are indirect recorded signals of brain [39, 12, 32].

Not many different methods have been proposed to estimate power spectral density. One way is to square the signal samples and average it over several realizations [31]. The most common method of estimating power spectral density is to square the amplitude of the spectro-temporal representation of a signal . We use analytic signal to compute power spectral density as follows: given $\hat{z}(t)$ is the complex-valued spectro-temporal representation of the estimated source signal $\hat{s}(t)$ in the lower beta frequency band, the instantaneous power of the source signal can be computed as below

$$\hat{p}(t) = \hat{z}(t)\hat{z}^*(t) = \hat{a}_z^2(t) \quad (3.5)$$

where $*$ denotes the complex conjugate. The average estimated power is given by

$$\bar{\hat{p}}(t) = \langle \hat{z}(t)\hat{z}^*(t) \rangle = \langle \hat{a}_z^2(t) \rangle \quad (3.6)$$

where $\langle \cdot \rangle$ denotes the time average.

To track the fluctuation of power over time, we average the instantaneous power over short time intervals and/or across trials. Temporal fluctuations of instantaneous

power of different signals at different locations are investigated so that sources whose power co-varies during a fast repetitive stimulus can be identified. In this study, we compute the instantaneous power of all the source epochs which are the responses to at least two stimuli moments. The stimulus is considered to be fast rate auditory stimulus which has previously been shown to make an ERS in several brain regions [12, 39] around the time of stimuli following a an ERD after the stimuli (ERD) in a MEG study. However, the rise of power occurs gradually when the next stimulus is approaching. This kind of source behavior may reflect the prediction of exact timing of the stimuli [12]. In this situation, the determination of baseline is a difficult task or may be impossible, because neural sources respond earlier than the stimuli during the period which is conventionally chosen as a baseline period. In Section 3.4, we will show how to localize dominant temporal power pattern in response to repetitive stimuli and localize the sources fluctuating with the corresponding temporal power pattern.

3.3 Coherence

A brain network may respond to stimuli by varying in the mutual phase information. In this case, power is not helpful, since there is no information of phase in the estimated power as in Eq 3.6. A complementary measure such as coherence, which is based on the phase relation consistency of sources, should also be taken into account. The complex-valued *coherency* between two source signals $\hat{s}_1(t)$ and $\hat{s}_2(t)$ at two different source locations with the corresponding analytic signals of $\hat{z}_1(t)$ and

$\hat{z}_2(t)$, respectively, is defined as below,

$$\hat{c}(t) = \frac{\langle \hat{z}_1(t) \hat{z}_2^*(t) \rangle}{\sqrt{\langle |\hat{z}_1(t)|^2 \rangle \langle |\hat{z}_2(t)|^2 \rangle}} \quad (3.7)$$

Still an absolute measure is needed to quantify the coherence among sources. Magnitude-squared coherence (MSC) was proposed by [2] and is computed as below

$$\hat{c}_{\text{ms}}(t) = |\hat{c}(t)|^2 = \frac{|\langle \hat{z}_1(t) \hat{z}_2^*(t) \rangle|^2}{\langle |\hat{z}_1(t)|^2 \rangle \langle |\hat{z}_2(t)|^2 \rangle} \quad (3.8)$$

By this measure, the sources are said to be perfectly coherent, if they have constant phase shift and constant amplitude ratio over a specified time interval/or trials. Spatial leakage of the spatial filtering to compute source time series is said to make artificial coherence due to zero phase shift (also called spurious coherence). Then, the real coherence is said to exist between two sources, if they have non-zero constant phase shift [38]. MSC cannot discriminate the coherence in terms of the value of the phase shift. In an MEG study, it was proposed to eliminate the zero-phase coherence with subtraction of MSC by its mean over time, which we call in this study as the mean subtracted MSC. The assumption is that if two sources are zero-phase coherent, their coherence has to remain constant. We show that this assumption is not true in all occasions and it is dependant on the amount of independent interference (see Section 3.3.1).

We propose to use the imaginary component IC of coherency $\hat{c}(t)$ denoted by $\hat{c}_{\text{ic}}(t)$ as an alternative to MSC measure. In our study, this measure is defined as the square of imaginary component

$$\hat{c}_{\text{ic}}(t) = (\Im[\hat{c}(t)])^2 \quad (3.9)$$

where $\Im\mathbf{m}[\cdot]$ denotes the imaginary part of a complex quantity. IC was originally used to remove volume conduction effect on the estimation of coherence of scalp sensor measurements. Application of IC was validated in the analysis of source space coherence [38]. IC has only non-zero value when computed between non-zero phase coherent signals and eliminates any spurious coherence due to zero-phase locked signals. It is shown mathematically in Section 3.3.1 and in the simulations (Chapter 4) that the imaginary component IC works superior to the mean subtracted MSC (explained earlier) [12] to cancel zero-phase coherence and detection of real coherence. The mathematical comparison of two measures are provided for the situation where the instantaneous signal-to-interference ratio (SIR) dynamically varies. In this research, we identify and localize the sources whose coherence with a reference source dynamically co-varies by examining the temporal coherence characteristics of $\hat{c}_{ic}(t)$ and $\hat{c}_{ms}(t)$. This kind of coherence identification is explained in Section 3.4.

3.3.1 Elimination of Common Source Coherence Effect

The ability of the two connectivity metrics MSC and IC to eliminate zero-phase coherence and to elaborate non-zero phase coherence is mathematically assessed here. The aim is to assess which measure is less sensitive to the artificial coherence due to the third source leakage. Can we eliminate artificial coherence obtained by MSC through subtracting off the MSC time average? This requires MSC caused by pure common source leakage to be constant over time. We test this assumption and compare it with the IC measure.

Model definition to show common source effect

Due to spatial filtering, two sources \hat{s}_i and \hat{s}_j at two different locations which are coherent due to a common source denoted by s_n are defined as below (for simplicity, we eliminate the dependency on time t)

$$\begin{aligned}\hat{s}_i &= \alpha_n s_n + \hat{n}_i \\ \hat{s}_j &= \beta_n s_n + \hat{n}_j\end{aligned}\tag{3.10}$$

where \hat{n}_i and \hat{n}_j are considered as the interference which may be due to the measurement noise or the interference of the other sources after spatial filtering. To clarify where the interference comes from, we use the original equations for the forward and inverse modeling as follows: Eq.2.2 in Chapter 2 expresses a typical estimated source located at q_0 as in terms of measurements below

$$\hat{s}(\mathbf{q}_0) = \mathbf{w}^T(\mathbf{q}_0)\mathbf{m}\tag{3.11}$$

\mathbf{m} is a linear combination of all sources (Eq.2.1) plus measurement noise \mathbf{n}

$$\mathbf{m} = \int \mathbf{a}(\mathbf{q}, \boldsymbol{\mu})s(\mathbf{q})d\mathbf{q} + \mathbf{n}\tag{3.12}$$

By substituting \mathbf{m} into Eq.3.11, $\hat{s}(\mathbf{q}, t)$ can be re-written as

$$\hat{s}(\mathbf{q}_0) = \int \mathbf{w}^T(\mathbf{q}_0)\mathbf{a}(\mathbf{q}, \boldsymbol{\mu})s(\mathbf{q})d\mathbf{q} + \mathbf{w}^T(\mathbf{q}_0)\mathbf{n}\tag{3.13}$$

Then, the summation of $\mathbf{w}^T(\mathbf{q}_0)\mathbf{a}(\mathbf{q}, \boldsymbol{\mu})s(\mathbf{q})$ ($\mathbf{q} \neq \mathbf{q}_0$) and $\mathbf{w}^T(\mathbf{q}_0)\mathbf{n}$ are considered as the total interference described in Eq.3.10 for each of the two sources separately.

Computation of MSC and IC

Now, we compute the MSC and IC coherence measures between the two sources. First, we derive the spectro-temporal representation as explained in the previous sections. We use a different notation for the spectro-temporal representation (which is a complex quantity) by replacing \hat{s} by \hat{z} for the source and \hat{n} by \hat{k} for the interference and re-express Eqs.3.10 as below

$$\begin{aligned}\hat{z}_i &= \alpha_n z_n + \hat{k}_i \\ \hat{z}_j &= \beta_n z_n + \hat{k}_j\end{aligned}\tag{3.14}$$

MSC denoted by \hat{c}_{ms} between the two sources is computed as below

$$\hat{c}_{\text{ms}} = \left| \frac{\langle \hat{z}_i \hat{z}_j^* \rangle}{\sqrt{\langle |\hat{z}_i|^2 \rangle \langle |\hat{z}_j|^2 \rangle}} \right|^2\tag{3.15}$$

We assume interferences and the source and also interferences themselves \hat{k}_i and \hat{k}_j are independent of each other, then the following expressions can be found

$$\begin{aligned}|\langle \hat{z}_i \hat{z}_j^* \rangle| &= \alpha_n \beta_n \langle |z_n|^2 \rangle \\ \langle |\hat{z}_i|^2 \rangle &= \alpha_n^2 \langle |z_n|^2 \rangle + \langle |\hat{k}_i|^2 \rangle \\ \langle |\hat{z}_j|^2 \rangle &= \beta_n^2 \langle |z_n|^2 \rangle + \langle |\hat{k}_j|^2 \rangle\end{aligned}\tag{3.16}$$

Finally, \hat{c}_{ms} is

$$\hat{c}_{\text{ms}} = \frac{\alpha_n^2 \beta_n^2 \langle |z_n|^2 \rangle^2}{[\alpha_n^2 \langle |z_n|^2 \rangle + \langle |\hat{k}_i|^2 \rangle][\beta_n^2 \langle |z_n|^2 \rangle + \langle |\hat{k}_j|^2 \rangle]}\tag{3.17}$$

We define signal-to-interference ratio as the ratio of signal power to the interference power and define three signal-to-interference ratios as below

$$\text{SIR}_i = \frac{\langle |z_n|^2 \rangle}{\langle |k_i^2| \rangle}, \text{SIR}_j = \frac{\langle |z_n|^2 \rangle}{\langle |k_j^2| \rangle}, \text{SIR}_{ij} = \frac{\langle |z_n|^2 \rangle}{\sqrt{\langle |k_j^2| \rangle \langle |k_i^2| \rangle}} \quad (3.18)$$

where $\sqrt{\langle |k_j^2| \rangle \langle |k_i^2| \rangle}$ is the geometric mean of the power of the two noise terms. \hat{c}_{ms} in Eq. 3.17 can be rewritten in terms of the three defined signal-to-interference ratios as below

$$\hat{c}_{\text{ms}} = \frac{\alpha_n^2 \beta_n^2 \text{SIR}_{ij}^2}{[\alpha_n^2 \text{SIR}_i + 1][\beta_n^2 \text{SIR}_j + 1]} \quad (3.19)$$

In the case of high signal-to-interference ratio (SIR) over the whole period of signals, the MSC tends to unity and therefore, is constant over time. When SIR tends to zero (high amount of interference), two signals become incoherent (MSC approaches zero). Generally, when SIR dynamically changes for any reason for instance due to an applied stimulus, thereby making MSC fluctuate. Then, elimination of the common source coherence is not possible by only subtraction of the time average of MSC (because of MSC fluctuation). IC measure denoted by \hat{c}_{ic} is a more rigorous measure to eliminate zero-phase coherence and is computed as below

$$\hat{c}_{\text{ic}} = \left[\mathfrak{Im} \left(\frac{\langle \hat{z}_i \hat{z}_j^* \rangle}{\sqrt{\langle |\hat{z}_i|^2 \rangle \langle |\hat{z}_j|^2 \rangle}} \right) \right]^2 \quad (3.20)$$

substitute Eq.3.16 into Eq.3.20 to find the final expression for \hat{c}_{ic} ,

$$\hat{c}_{\text{ic}} = \left[\mathfrak{Im} \left(\frac{\alpha_n \beta_n \langle |z_n|^2 \rangle}{\sqrt{\langle |z_i|^2 \rangle \langle |z_j|^2 \rangle}} \right) \right]^2 \quad (3.21)$$

where \hat{c}_{ic} goes to zero because the coherence does not have any imaginary component because of common signal in both sources. This mathematical proof shows that zero-phase coherence can be eliminated without any dependency on SIR, if IC is used, while MSC depends on the amount of interference.

3.4 Localization of Network

So far, the methods to compute instantaneous power and coherence have been introduced. In this section, the most dominant temporal power pattern and the most dominant temporal coherence pattern are identified and the corresponding sources are localized based on Singular Value Decomposition (SVD). In a similar way, few studies have focused on the analysis of temporal dynamics of coherence and power during fast rate stimuli [12, 39, 44]. In particular, common temporal pattern of power has been identified in the beta frequency band among several specific cortical and subcortical sources during fast repetitive auditory stimuli [12] based on MEG measurements. The similar synchronization/desynchronization pattern in centro-frontal regions of brain has been found in a surface EEG study. A periodic temporal pattern of coherence at the frequency of stimuli has also been observed in a recent study with MEG [12], where principal component analysis (PCA) was used to detect it. Here, we present the steps to localize sources underlying common temporal pattern of power and coherence in the source space solution estimated from EEG measurement during fast auditory stimuli. For this purpose, SVD is directly applied to the power and coherence data of source space to detect similar pattern networks. Such a technique was applied in the same context as previously proposed [10] to detect the correlated network. This is carried out as follows:

Two *feature matrices*, denoted by $\hat{\mathbf{D}}_p, \hat{\mathbf{D}}_{i\varepsilon}$ consisting of samples of the power temporal patterns and the coherence temporal patterns, respectively, are constructed. Each row of $\hat{\mathbf{D}}_p$ consists of T time bins of power samples of each source obtained by Eq.3.6. Since there are N number of sources, then, $\hat{\mathbf{D}}_p$ is a $N \times T$ matrix. Each row of $\hat{\mathbf{D}}_{i\varepsilon}$ consists of T time bins of coherence samples of each source with respect to a fixed reference source with index i . Two different kinds of coherence measures $\hat{c}_{ms}(t)$ (mean subtracted $\varepsilon = ms$) and $\hat{c}_{ic}(t)$ ($\varepsilon = ic$) as given by Eqs.3.8 and (3.9) are employed. Since both $\hat{\mathbf{D}}_{i\varepsilon}$ and $\hat{\mathbf{D}}_p$ are $N \times T$ matrices, for simplicity, we use a common notation $\hat{\mathbf{D}}_s$ for both feature matrices in the following discussion. Singular Value Decomposition is applied on $\hat{\mathbf{D}}_s$ as below

$$\hat{\mathbf{D}}_s = \hat{\mathbf{U}}\hat{\mathbf{\Lambda}}\hat{\mathbf{V}}^T \quad (3.22)$$

where $\hat{\mathbf{U}}$ and $\hat{\mathbf{V}}$ contain left and right singular vectors, respectively. $\hat{\mathbf{\Lambda}}$ is a $N \times T$ matrix consisting of the associated singular values. The first column of $\hat{\mathbf{U}}$ ($\hat{\mathbf{u}}_1$) is the first principal component coefficients corresponding to the first column of $\hat{\mathbf{V}}$ ($\hat{\mathbf{v}}_1$). In the principal component analysis (PCA), they are known as the first loading and the first score, respectively. In this study, $\hat{\mathbf{u}}_1$ refers to the first principal source distribution corresponding to $\hat{\mathbf{v}}_1$ the first principal and the most prominent temporal pattern. We show below that how these quantities are related and why they provide such information about the underlying source distribution and the temporal pattern. First, multiply the two sides of Eq.3.22 by $\hat{\mathbf{V}}$. Since $\hat{\mathbf{V}}$ is an orthonormal matrix ($\hat{\mathbf{V}}^T\hat{\mathbf{V}} = \mathbf{I}$), we can write down as below, if the only first columns $\hat{\mathbf{U}}$ and $\hat{\mathbf{V}}$ are

considered

$$\hat{\mathbf{D}}_s \hat{\mathbf{v}}_1 = \hat{\mathbf{u}}_1 \hat{\lambda}_1 \quad (3.23)$$

where $\hat{\lambda}_1$ is the corresponding first singular value. Since the norm of $\hat{\mathbf{u}}_1$ is unity, then $\|\hat{\mathbf{D}}_s \hat{\mathbf{v}}_1\|_2 = \hat{\lambda}_1$. As a result, $\hat{\mathbf{u}}_1$ can be expressed as below

$$\hat{\mathbf{u}}_1 = \hat{\mathbf{D}}_s \hat{\mathbf{v}}_1 / \|\hat{\mathbf{D}}_s \hat{\mathbf{v}}_1\|_2 \quad (3.24)$$

where $\|\cdot\|_2$ denotes 2-norm of a matrix or vector. Eq.3.24 clarifies how coefficients of $\hat{\mathbf{u}}_1$ are simple dot product between the rows of feature matrix (containing temporal power and coherence measure) and $\hat{\mathbf{v}}_1$, the first principal temporal pattern, multiplied by the reciprocal of the constant, $\|\hat{\mathbf{D}}_s \hat{\mathbf{v}}_1\|_2$. Note that rows of the feature matrix should not be normalized, because the strength of power and coherence need to be considered besides their temporal fluctuations. Finally, thresholding $\hat{\mathbf{u}}_1$ simply localizes sources with the most prominent temporal pattern either in spectral power or coherence. The network consisting of sources detected based on power data is called POW-NET and the one based on coherence data samples is called COH-NET.

Chapter 4

Implementation

So far, we have explained the procedure to estimate brain source signals and identify the similar power and coherence temporal patterns in the source space, given EEG scalp measurements. In this Chapter, we present the results of method implemented on simulated and real data. Firstly, a comparison is made between the mean subtracted magnitude-squared coherence (MSC) and the imaginary component (IC) to distinguish between nonzero phase-locked coherence and zero-phase locked coherence. Synthetic EEG data is generated given simulated brain sources located in a template head model. Spatial filtering is then performed on the scalp EEG data to estimate source time series in a previously defined region known as source space, which is restricted to grey matter (extracted from MRI). The effect of correlation among sources on the output of the spatial filter is assessed and it is shown that the solution can be improved by a proper choice of data samples in the calculation of covariance matrix. POW-NET and COH-NET are then calculated based on Chapter 3 and the results of procedure are illustrated for the computer generated data.

Recognition of dynamic neural responses which change in coherence and power is

made using real EEG data. Data is recorded from three subjects who are passively listening to repetitive tones at rates 1.2Hz, 1.7Hz, and 2.5Hz. POW-NET and COH-NET are recognized and compared to the previous studies. We will show that dynamic coherence and power changes can be identified with EEG and localization can also be made to recognize the neural sources at higher spatial resolution than as what is found by scalp EEG data.

4.1 Simulation

4.1.1 Comparison of Coherence Measures

In Chapter 3, we have shown mathematically that imaginary component (IC) performs superior to mean subtracted MSC to eliminate zero phase-locked coherency irrespective of instantaneous SIR in this scenario. As it was shown, MSC remains constant only if SIR stays constant over time or goes to infinity (where MSC tends to unity and stays constant). We elaborate this fact in the computer simulations and confirm the results of the theoretical comparison. Therefore, the aim here is to compare the performance of the two coherence measures in the recognition of nonzero phase-locked coherency and elimination of zero phase-locked coherency. For this purpose, two signals are generated in two different conditions and coherence is instantaneously computed with the two measures as illustrated in Figure 4.1. The temporal envelope of the signals is the same and corresponds to the one shown in Figure 4.4.(a), but their instantaneous phase varies in the following way. In the first condition, the two signals are nonzero phase-locked at particular instants of time and non phase-locked at other instants. To do so, coherency is made if the envelope of

the signals becomes less than 0.8 and the phase difference is $\pi/4$. In the second condition, the two signals are entirely zero phase-locked. The instantaneous phase of non phase-locked instants for the first condition is randomly and uniformly chosen from the range $[0, 2\pi]$. Based on Eq.3.10, we add noise to the source signals to mimic the interference of other sources due to spatial filtering. The total interference as a result of other interfering source signals and the model noise is considered to be independently, randomly distributed samples from Gaussian distribution. The noise is assumed to follow the same distribution in both signals with zero mean and variable standard deviation which leads to the variable instantaneous SIR as sketched in Figure 4.1.(c). For each source, 100 trials are generated. Figure 4.1.(a) and Figure 4.1.(b) show the two instantaneous coherence measures (MSC (blue) and IC (red)) overlaid on each other for the first and the second conditions, respectively. As expected, both measures show fluctuations of coherence over time in the first condition, so that the nonzero phase-locked activity is contrasted by having higher values with respect to non phase-locked periods. But in the second condition, where the two signals are entirely zero-phase locked, the MSC does not remain constant and fluctuates with changes in the instantaneous SIR illustrated in Figure 4.1.(c). Therefore, coherence cannot be eliminated by just subtracting the mean of MSC. But, IC performs superior to eliminate the zero phase-locked coherence and is not dependant on the instantaneous SIR in this scenario. Figure 4.2 shows the magnitude-squared measure versus different values of signal-to-interference ratio based on Eq.3.19 derived in Chapter 3, where the two signals are considered to be entirely zero phase-locked. To plot this Figure, $\alpha_n = \beta_n = 1$ and $SIR_i = SIR_j = SIR_{ij} = SIR$. Figure 4.1 and Figure 4.2 confirm the fact that magnitude-squared coherence between two zero-phase locked

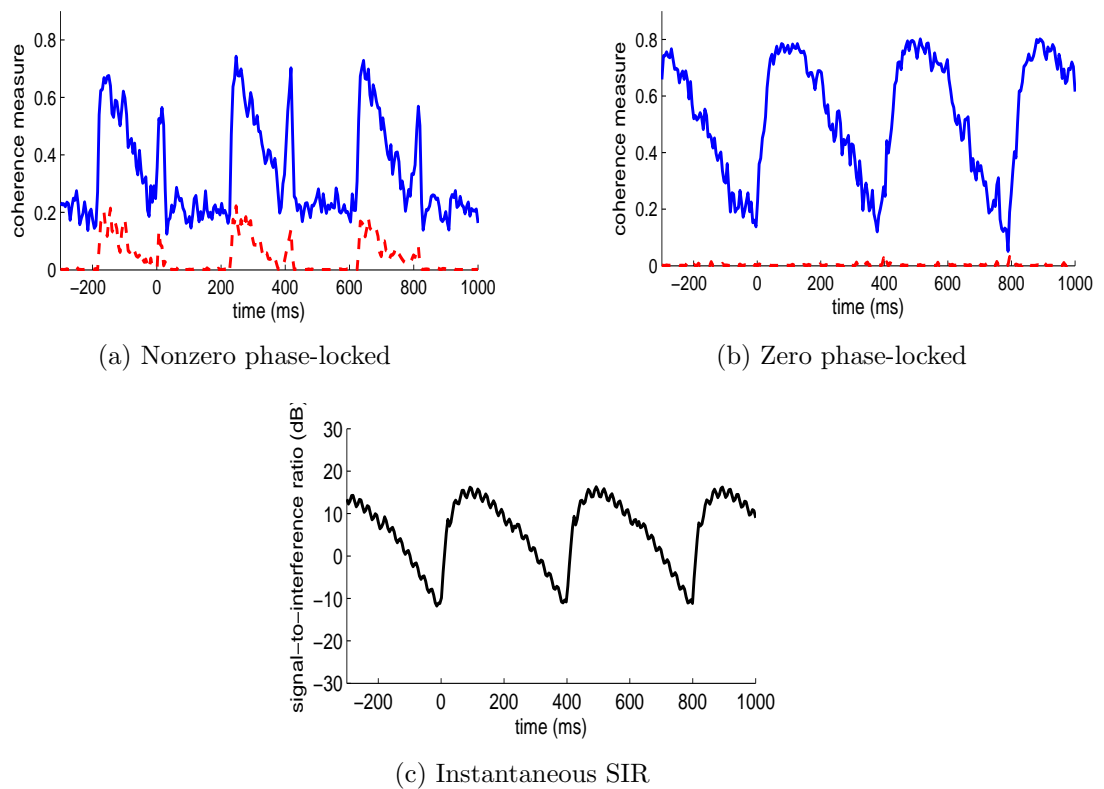


Figure 4.1: Instantaneous measure of coherence by MSC (blue) and IC (red). Bottom is the instantaneous SIR of the two signals (see text for more details).

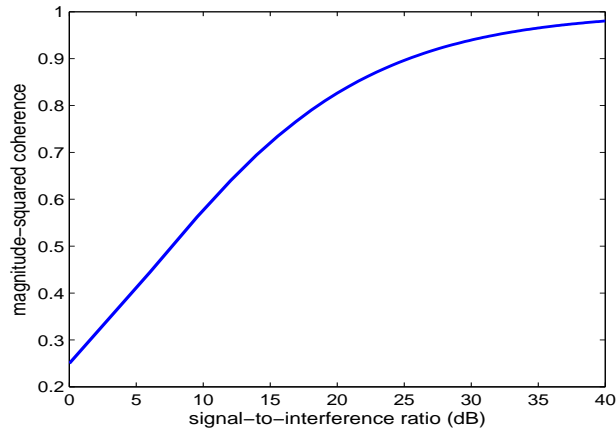


Figure 4.2: Dependency of MSC on SIR when two signals are entirely zero phase-locked.

signals will not be constant over time, if the signal-to-interference ratio varies.

4.1.2 Head Model and Spatial Filtering

From this point to end, we present the results of simulations and analysis of real data to study the dynamic changes of statistical coherence and power of neural sources. In this section, we explain the procedure taken to prepare the forward and inverse model which are the same for simulations and real data. The anatomy used for the simulations is MNI/Colin27 with 1mm resolution. The cortex, cerebellum and white matter surfaces are extracted with BrainVISA software. The vertices of the cortex surface were triangulated and resampled leading to 5005 vertices defined as possible source positions. 128 evenly distributed sensors based on Biosemi configuration are used to simulate EEG sensors. The location of sensor array is fitted to the standard anatomy. Forward model is built with Brainstorm [42], which is

documented and freely available for download online under the GNU general public license (<http://neuroimage.usc.edu/brainstorm>). In this software, boundary element method (BEM) is used to build the electric leadfield matrix [16]. To implement BEM, 1082 vertices and 642 vertices are used for the scalp and the skull, respectively. The conductivity ratio of skull to scalp is set to 0.0125. Further analysis including spatial filtering is performed with MATLAB. To perform spatial filtering, appropriate calculation of the covariance matrix is needed. In the next section, we show the effect of correlated sources on the reconstructed waveforms.

4.1.3 Effect of Correlated Sources

We simulate two sources in the left and right auditory cortices ¹ with *Talairach* coordinates (-42,-22,2mm) and (40,-24,2mm) having a signal waveform such as the one shown in Figure 4.4.(a) (To know about Talairach coordinate system ², please see Figure 4.3 and refer to [43] for more information). The orientation of the two sources is constrained to be normal to the cortical surface. EEG data is generated based on forward model explained above. Gaussian noise is added to the EEG signals to make SNR=5 dB. SNR is computed as the ratio of average signal power to the average noise power. A total of 130 trials are generated, each consists of a window in the range [-300,1000ms] with the sampling frequency set to 200Hz. We show the effect of source correlation on the reconstructed source signals obtained by the spatial filtering method explained in Chapter 2. The source waveforms of the two auditory

¹a region of cerebral cortex which processes sound and is located in the temporal lobe (one of the four lobes of cerebral cortex).

²Talairach coordinate system is established by Jean Talairach to define anatomical structures of brain, regardless of individual differences in brain size and shapes. It is based on two points named anterior commissure (AC) and posterior commissure (PC), and also a vertical plane called midsagittal plane illustrated in Figure 4.3.

sources correspond to Figure 4.4.(a) which change in power maybe due to several repetitive auditory stimuli. The left column in this figure shows the reconstructed source waveform of the right auditory source when it is perfectly correlated (zero phase-locked) with the source in the left auditory cortex during the period when the envelope of signals is less than 0.8 (in a periodic manner). The right column is the reconstructed source waveform for the case where the sources have nonzero phase-locked correlation at the same moments (phase difference= $\pi/4$). Figures 4.4.(b,c,d) show the reconstructed source waveform for different windows chosen to estimate covariance matrix. In Figure 4.4.(b), the covariance matrix is calculated by a snapshot of data over trials within the period that two sources are correlated either zero phase-locked or nonzero phase-locked. In Figures 4.4.(c), the covariance matrix is estimated by choosing a data snapshot outside the correlated period. In Figures 4.4.(d), the covariance matrix is calculated over all snapshots and trials. As it is clear, the source waveform is preserved and not distorted in the two situations if the covariance is computed over all snapshots and trials including both correlated and uncorrelated periods. In the same way, we use all snapshots over trials to compute the proper covariance matrix for the analysis of simulated and experimental data.

Regularization constant is the other important parameter affecting the spatial filtering solution. Care must be taken to choose an appropriate value for regularization constant. It will be explained in more details in Section 4.1.6.

4.1.4 Analysis of Performance

We test the localization ability of the explained procedure in Chapter 3 to localize power-based and coherence-based distributed networks (POW-NET and COH-NET).

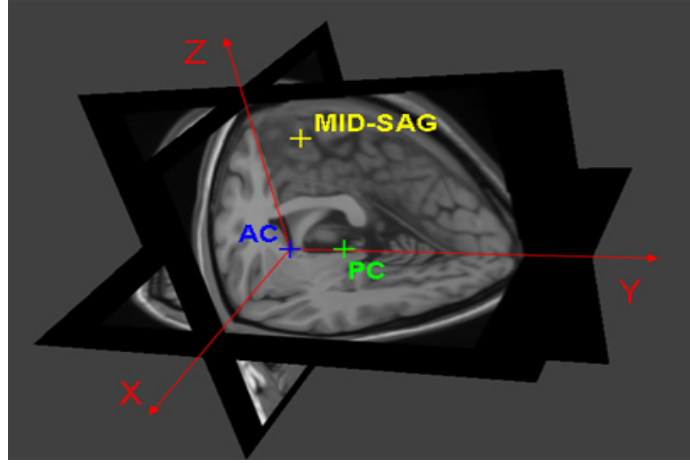


Figure 4.3: Talairach coordinate system, three main components of it are AC, PC and the vertical midsagittal plane. The image is from Center for Information Technology (CIT) (<http://mipav.cit.nih.gov>).

Two parameters localization error (E_l) and normalized burring index (NBI) are employed to assess localization accuracy and spatial resolution. The localization error is defined here as the distance between the source of maximum strength and the true simulated source within a sphere surrounding the simulated source. The normalized burring index measures how an estimated source is spatially spread within a sphere surrounding the true simulated source [18]. The formula to calculate NBI is expressed as below

$$\text{NBI}_k = \frac{\sqrt{\frac{\sum_i \|\mathbf{r}_i - \mathbf{r}_k\|^2 \mathbf{u}^2(i)}{\sum_i \mathbf{u}^2(i)}}}{\sqrt{\frac{\sum_i \|\mathbf{r}_i - \mathbf{r}_k\|^2}{\sum_i 1}}} \quad (4.1)$$

where \mathbf{r}_k is the position of true source with index k , \mathbf{r}_i is the position of estimated source with index i within the sphere and $\mathbf{u}(i)$ is the intensity of the estimated source. As the estimated source is spread in the region of interest, the NBI is closer to 1 and if sharply distributed, the NBI is close to zero. E_l and NBI are calculated in a sphere

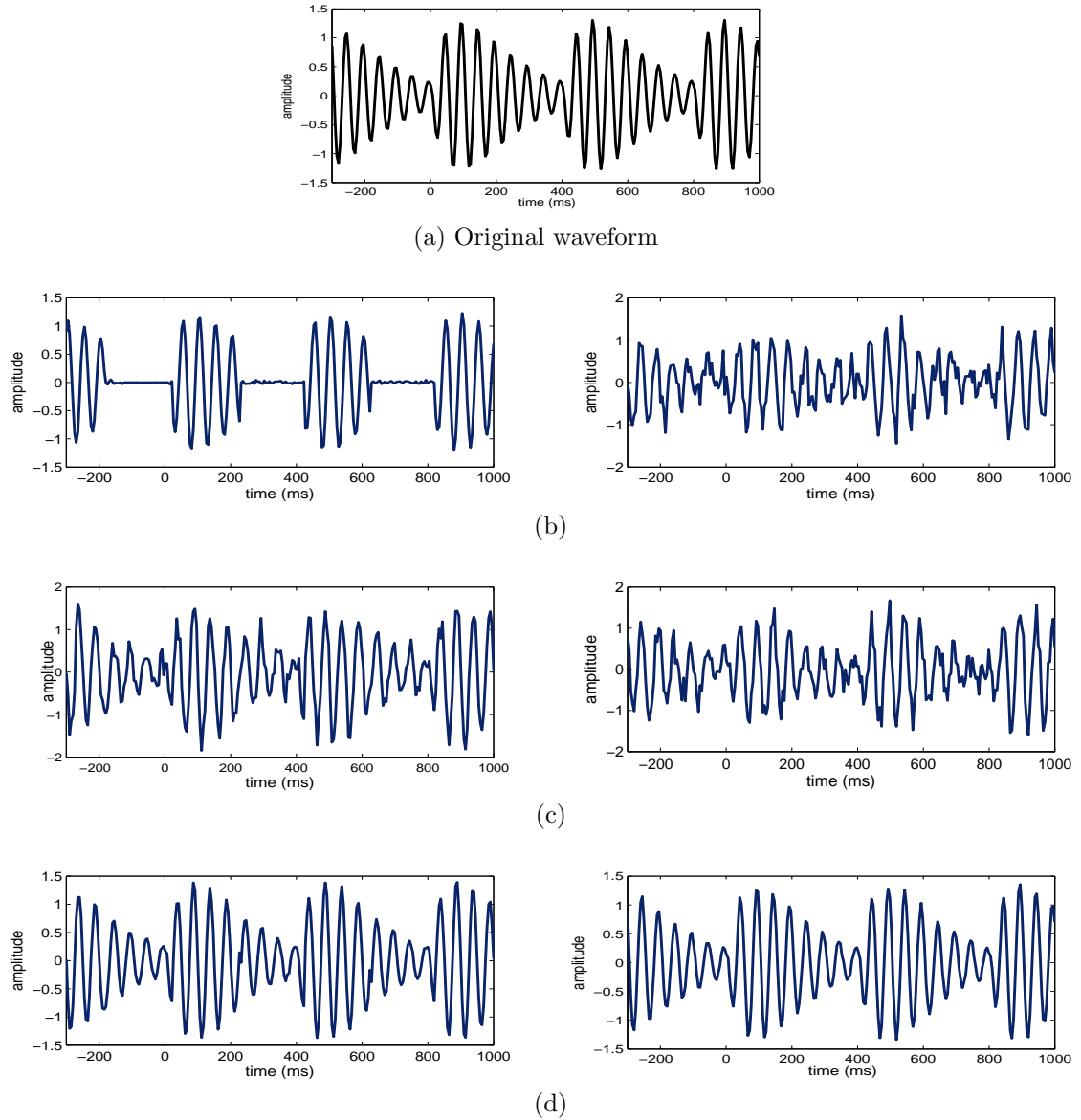


Figure 4.4: (a) Original waveform of the right auditory source. (b,c,d) the reconstructed waveform by different estimated covariance matrices. Covariance matrix is computed (b) at the snapshot when the sources are correlated, (c) uncorrelated, (d) over the whole period. Left column: correlation due to zero phase-locked coherency, and right column: correlation due to nonzero phase-locked coherency.

surrounding the true source location where the radius of sphere is chosen to be 26mm.

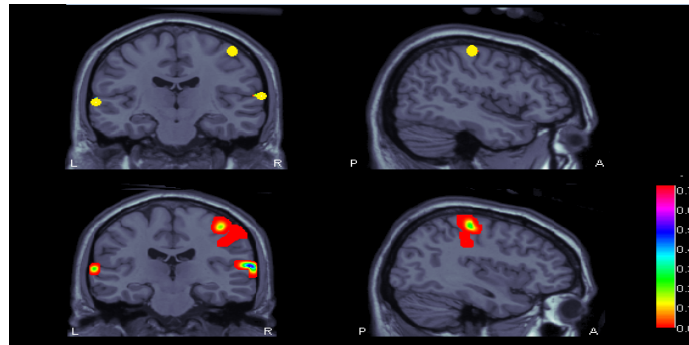
4.1.5 Detection and Localization of Power Response to Repetitive Stimulation

In this section, we want to examine the ability of the explained procedure to detect dynamic changes in power and the accuracy of the corresponding spatial localization (POW-NET). To do so, three sources are simulated in three different locations in brain as explained below. They all have the same waveform corresponding to the one showed in Figure 4.4.(a). Their instantaneous phase difference is considered to be constant where the amplitude of signals is less than 0.8 and random otherwise. EEG signals are simulated with BEM and source waveforms are estimated as explained in the section 4.1.2. Instantaneous power of sources is then estimated after applying Hilbert transform and obtaining associated analytic signals. The data matrix $\hat{\mathbf{D}}_s$ is then formed and the first principal temporal pattern and the corresponding source distribution is obtained by Eq.3.23 and Eq.3.24. Two configurations, found in the previous studies to be involved in the mechanism of dynamic power co-changes with fast repetitive auditory stimuli [12, 32], are chosen to assess the method. Figure 4.5 displays the localization results of estimated POW-NET locations based on the the first principal component explained in Chapter 3. The first configuration consists of superficial sources located in the left and right superior temporal gyrus, and left precentral gyrus (Figure 4.5.(a)). Figure 4.5.(a) (upper row) shows the true source locations and the lower row of this figure consists of the first estimated principal source distribution. Figure 4.5.(b) (lower row) shows the localization results of the second configuration where the sources are located in deeper regions including supplementary

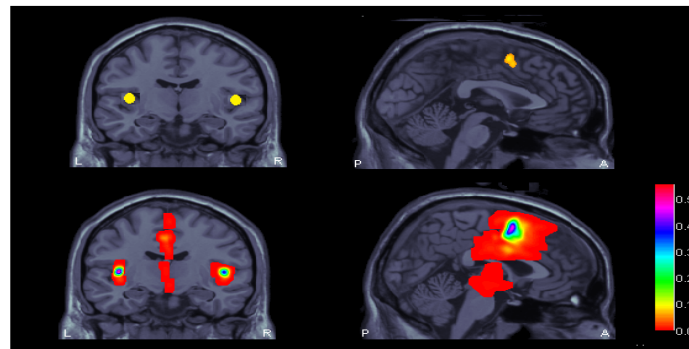
motor area, left and right insula (true source locations are displayed in the upper row). The figures show the efficiency of the algorithm to identify true POW-NET locations (as shown in the upper rows of both figures). Both figures give almost a focal distribution of the estimated sources around the true sources locations. Localization error E_l is obtained zero in both configurations and the value of NBI is 0.0059, 0.0017, and 0.0042 respectively for the precentral, left and right temporal sources in the superficial source configuration and is 0.0178, 0.0048, and 0.1105 for the left and right temporal sources, and SMA in the deep source configuration.

Figure 4.6 shows the results of the localization algorithm implemented for a mixed configuration. Upper row of Figure 4.6.(a) shows the true source locations. The second and third rows of it show a comparison of results in different additive noise situations making SNR=5dB and SNR=-5dB, respectively. The second row corresponding to the higher SNR illustrates a higher resolution image of the first principal component source. When the SNR is lower as in the third row, a wider spread of source activity is obtained. The localization error is obtained zero again for the three sources and NBI is found to be 0.1137, 0.011, and 0.0037 for the SMA, the left and right temporal lobe sources respectively in the higher SNR situation and 0.3424, 0.0191, and 0.0549 in the lower SNR situation. The results of NBI and estimated source image show that in a high noise condition, the sources are wider spread over the true source region specially for the source located in SMA for its higher SNR.

The first principal temporal pattern of the estimated source and the instantaneous power of true source are computed as explained in Chapter 3. Instantaneous power of true sources is computed in the same way as done for estimated sources. The true power signal (solid, red curve) is overlaid on the first principal component of estimated



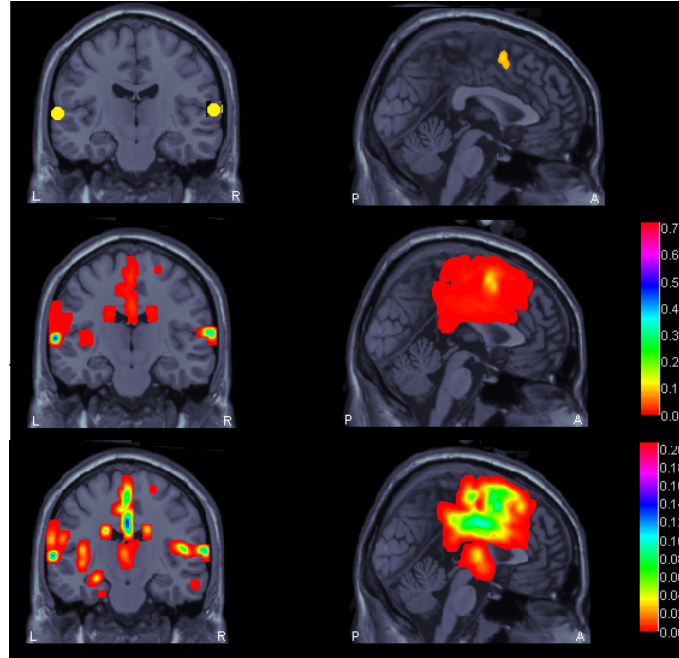
(a) Superficial sources



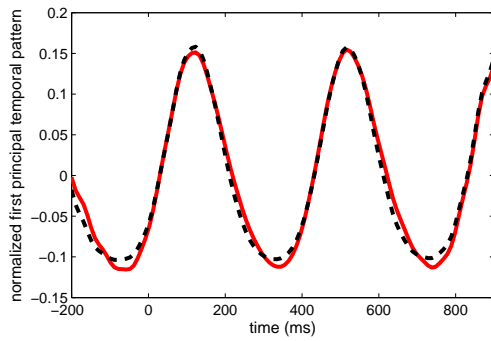
(b) Deep sources

Figure 4.5: Results of the localized sources obtained by power estimation and the subsequent singular value decomposition in two different configurations. Two views of MRI, coronal (view from back) and sagittal (view from side), are displayed.

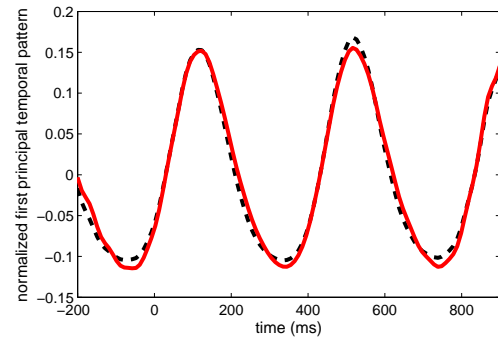
power signals (dashed, black curve) as shown in Figure 4.6.(b) (for SNR=5dB) and Figure 4.6.(c) (for SNR=-5dB). The true power signal is projected onto the estimated power pattern. The two figures, Figure 4.6.(b) and Figure 4.6.(c), correspond to the second and the third rows in the estimate image of POW-NET. Dynamic changes of power can be properly reconstructed with the procedure to localize the POW-NET. No serious distortion in the waveforms is observable, even when the amount of noise changes.



(a)



(b)



(c)

Figure 4.6: Effect of SNR on the reconstructed mixed configuration of superficial and deep sources in power analysis. (a) Upper : true source locations shown by yellow spots and source distribution for Middle : $\text{SNR} = 5\text{dB}$, and below: $\text{SNR} = -5\text{dB}$ (the same MRI views as Figure 4.5 displayed). (b,c) Dominant temporal pattern of estimated power (solid, red curve) when (b) $\text{SNR} = 5\text{dB}$ (c) $\text{SNR} = -5\text{dB}$ overlaid by true power pattern (dashed, black curve).

4.1.6 Detection and Localization of Coherency Response to Repetitive Stimulation

The second type of localization as discussed in this thesis is based on coherence analysis and the associated network is called COH-NET. We simulated three superficial sources in the same locations as shown in Figure 4.5.(a) (upper row) for power-based localization (right precentral gyrus, left superior temporal gyrus, right superior temporal gyrus). The source waveforms are the same as the ones used in the power analysis. We made a periodically dynamic coherency between the sources in the right precentral gyrus and in the left superior temporal gyrus. In addition, a non-coherency between the source in the right superior temporal gyrus and the two other sources is made. To do these, the phase difference between the two periodically coherent source signals is maintained constant over trials as the envelope of the waveforms falls less than 0.8 and otherwise the individual phase is chosen randomly from a uniform distribution $[0, 2\pi]$. The instantaneous phase of the right temporal gyrus is entirely chosen randomly from the uniform distribution at all moments and trials, thereby making it entirely non-coherent with the other two sources. This kind of source configuration simulates stimuli dependant neural responses, that the coherent periods may be the time when cortical and subcortical networks interact in response to repetitive stimuli.

We use the same procedure for forward model as in the previous simulations. Then, we apply the spatial filtering to estimate source time series of all 5005 sources in the brain. Thereafter source waveforms are computed, instantaneous coherence is obtained between all sources with a reference source, where here it is chosen to be the precentral gyrus source. All the coherence waveforms are stacked in the rows of data matrix $\hat{\mathbf{D}}_s$ and then based on Eq.3.23 and Eq.3.24, the coherence temporal

waveforms and the first principal temporal pattern of coherence and the corresponding source positions are obtained and displayed in Figure 4.7 and Figure 4.8. We use two coherence measures (1)- mean subtracted magnitude-squared coherence (MSC), (2)- imaginary component (IC). We analyze the localization performance with localization error and NBI, as used for the power analysis section.

In Figure 4.7, each subfigure corresponds to the source distribution of the first principal component (right obtained by IC and left by MSC). Figure 4.7.(a) shows the results of singular value decomposition on the coherence data obtained from true source signals. We have added random Gaussian samples (zero mean and standard deviation of 0.01 times the amplitude of true source) to all the vertices, which makes it possible to use singular value decomposition on the coherence temporal samples of all defined as source space. The reference source is shown with a white solid circle overlaid on the coefficients of the first principal component and the true coherent source location is indicated with a cross hair. Now, we assess the performance of the localization method to localize the coherent source and detect the true coherence waveform. Figure 4.7 (b,c) and Figure 4.7 (d,e) show the results of reconstructed source image corresponding to the first principal component, where SNR is equal to 15 dB and 5 dB, respectively. Two different regularization constants (α) are used in the inverse method to show the role of regularization in the localization results besides the effect of SNR. As shown in this figure, in higher SNR, the coherent source is more accurately and focally obtained ($E_l = 0$, NBI = 0.67) by IC measure in comparison to MSC ($E_l = 12.90mm$, NBI = 0.97), if α is low enough. If α is greater in the same SNR case, both measures have a localization bias and spatially spread representation of the true source (for IC $E_l = 17mm$, NBI = 0.98) and (for MSC $E_l = 14mm$,

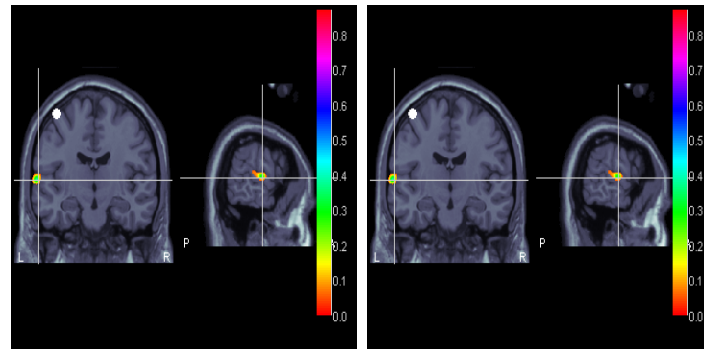
NBI = 0.99). However, it can be visually found that a more concentrated pattern is formed around the source when obtained with IC metric rather than MSC, in this case more (more observable in the sagittal view). In the lower SNR situation and lower regularization, the true source position is more accurately detected with IC measure and is less spread ($E_l = 0$, NBI = 0.71) than what is obtained by MSC ($E_l = 23mm$, NBI = 0.99). When α is increased, both measures do not localize the source in its true position leading to a bias expressed by E_l which is $18mm$ for IC and $12mm$ for MSC. The two reconstructed source images show widely spread of activity around the true coherent source where NBI is 0.99 for IC and 0.98 for MSC. However, the source image again represents a more concentrated distribution around the true source, when obtained by IC measure rather than MSC (again more obvious in the sagittal view).

Figure 4.8 illustrates the first principal temporal pattern of coherence corresponding to the source distribution shown in Figure 4.7. The first row shows the principal temporal pattern of coherence obtained from original source waveforms. As in Figure 4.7, left corresponds to MSC temporal pattern and right corresponds to IC temporal pattern. The same fluctuations as the original coherence waveform are observable with the two coherence measures IC and MSC in all cases except for the case where the SNR is low and regularization constant is chosen to be low relative to λ_{max} . It confirms the precious role of regularization constant in a low SNR situation to improve signal-to-noise ratio of the spatial filtering output. But, we need to note that α always makes a trade-off between output SNR and spatial resolution. We clarify this fact by comparing the last row of Figure 4.7 (source distribution) and Figure 4.8 (the corresponding temporal pattern of coherence). By IC-based localization, a focal

source activity is obtained with zero localization error in the position of original source in the low regularization. However, the coherence waveform is strongly distorted in this case. In contrast, high regularization constant leads to less spatial resolution but preserves the source coherence temporal pattern with seed source. By MSC-based localization, although the result of low regularization constant is not as focal as the one obtained IC, but still has focal distribution of source around the true source position when compared with higher regularization. Also with lower regularization, the coherence waveform is distorted with both MSC and IC measures. Therefore, higher regularization helps to improve the reconstruction of periodic fluctuations of coherence but it also leads to biased localization error. In addition, low amount of regularization has led to zero localization error with IC metric, but MSC measure always resulted in a biased localization error. In summary, we should choose an appropriate amount of alpha to make a compromise between output signal-noise-ratio and the spatial resolution.

4.2 Real EEG Data

As we have already shown in the Section 4.1, implementation of beamforming method and subsequent source analysis such as power and coherence on EEG signals can lead to detection and localization of power-based and coherence-based networks in response to a certain stimulus. An EEG experiment is performed to show how dynamic changes in power and coherence can be detected based on EEG signals. In this experiment, repetitive auditory stimuli are played and subjects are passively listening to them. The time interval between stimuli is around the tempo which is optimum for musical perceptions 1.2, 1.7, and 2.5Hz [44]. Previous studies have shown that motor regions



(a) Coherent sources

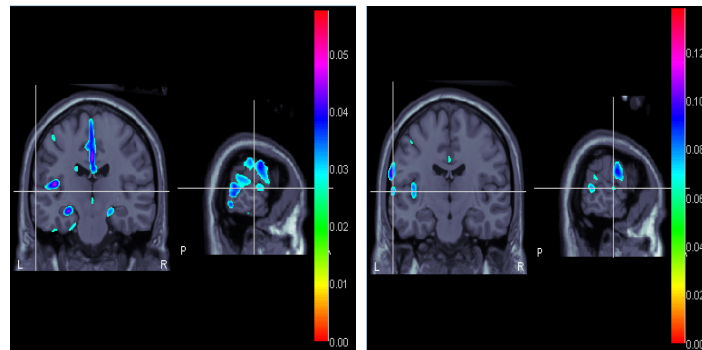
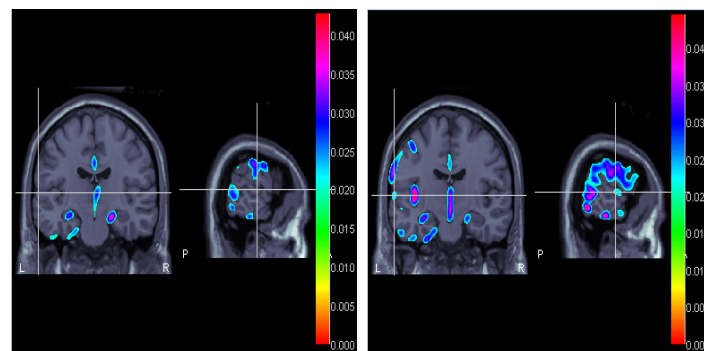
(b) SNR = 15dB, $\alpha = 0.001\lambda_{max}$ (c) SNR = 15dB, $\alpha = 0.01\lambda_{max}$

Figure 4.7: Continued on the next page.

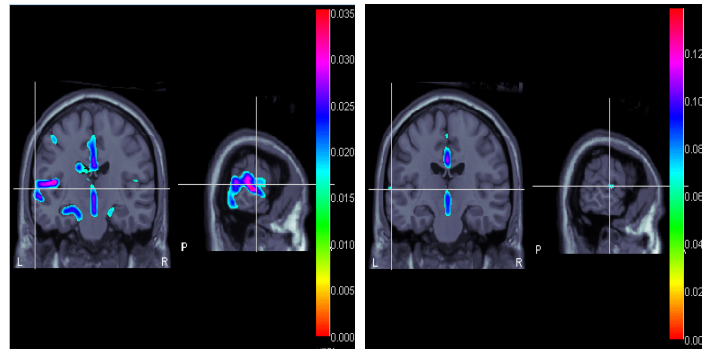
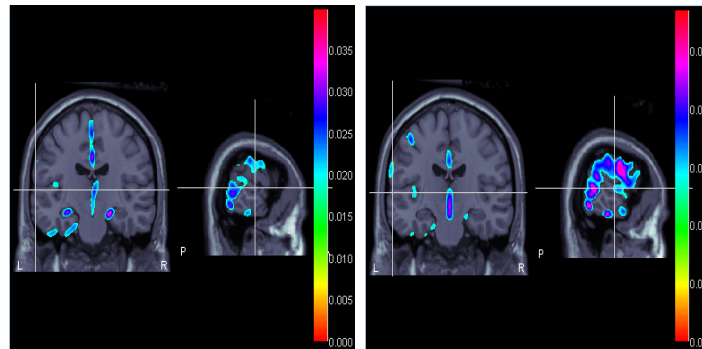
(d) SNR = 5dB, $\alpha = 0.001\lambda_{max}$ (e) SNR = 5dB, $\alpha = 0.01\lambda_{max}$

Figure 4.7: Source distribution corresponding to the first principal component obtained by IC and MSC metrics. In each subfigure, left: corresponding MSC and right: corresponding IC. (a): True distribution (reference source shown by a white solid circle and the coherent source by a cross hair), (b,c): Reconstructed source distribution for SNR = 15 and the varying regularization constant, (d,e): Reconstructed source distribution for SNR = 5 and also the varying regularization constant. Color bar shows the intensity of the first principal component coefficients. The same MRI views as Figure 4.5 are displayed.

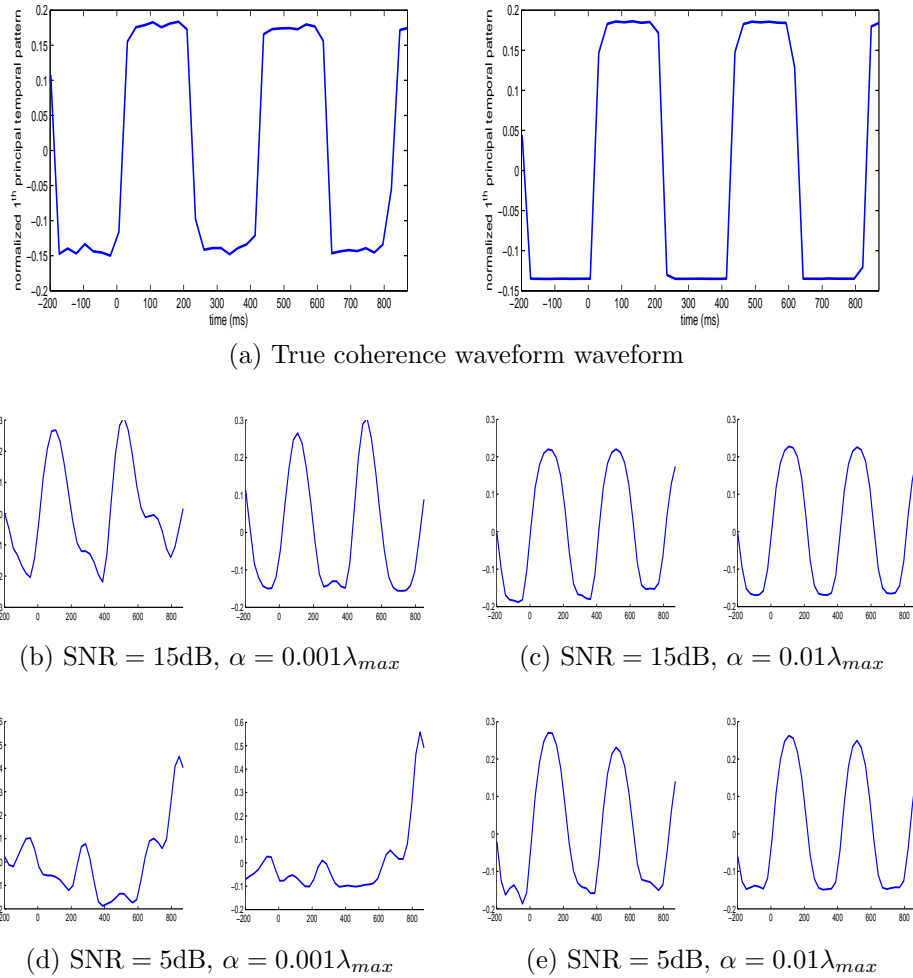


Figure 4.8: The first principal coherence waveform of the source distributions shown in Figure 4.7.

of brain are recruited in perception of musical rhythms [6],[15],[12], even when no movement is performed. The recent study with MEG [12] showed dynamic coherence exist between auditory and motor regions. The aim of this study is to show such dynamic coherence based on the explained procedure to extract principal pattern of coherence, only based on EEG data. We choose auditory source as the most probable source in response to auditory stimuli and analyze the coherence of other sources with respect to this source. Therefore, we need to find the position of such a source as the first step. The source of auditory potential has been localized and in various studies [33],[14] or [19]. These studies used auditory evoked potential measured from scalp surface and localized the auditory source by different localization methods such as spatio-temporal algorithm [14], synthetic aperture magnetometry (SAM) [19], and dipole source analysis [33]. Evoked potential is obtained by averaging channel responses over enough number of trials. The averaging filters out noise and all the other responses which are not phase locked to stimuli and leads to several important peaks known as P1 (50ms) and N1 (100ms). The method we use to localize the auditory source or sources is somewhat similar to SAM and is based on finding the prominent source or sources with similar dynamic power changes, as will be described in Section 4.2.2. The similarity with SAM comes from the fact that beamforming is used in this method as is also used in SAM. After auditory source is detected, we will compute the instantaneous coherence between this source and all the other sources and detect the major coherence pattern and the corresponding sources by singular value decomposition (see Section 4.2.3). We apply this procedure with two coherence metrics IC and MSC and compare the results of the two metrics with the previous studies on the perception of musical beats. We show the the power

of IC to cancel out spurious coherence and compare the coherence temporal pattern of both metrics. To the best of author's knowledge, this is the first study with EEG to localize dynamic changes of coherence with auditory source in response to a train of musical beats.

4.2.1 Procedure of Experiment and Preprocessing

Three students from McMaster University, aged 19-28 (mean 24.7, 1 left-handed, all female) volunteered to participate in the experiment. All participants gave informed consent by signing a consent form approved by the Research Ethics Board of McMaster University. Normal hearing status is verified via threshold audiometry (GSI-61 audiometer) to 8kHz for each participant. Participants sat in a chair placed 1.4m in front of a computer monitor in a sound attenuated (ambient noise 16dBA) electrically shielded booth. Participants watched a silent video of their choice with subtitles enabled for the duration of the experiment. Individual stimuli are pure tones at 264Hz, duration 45ms including an 8ms rise/fall time, presented binaurally at 80dB SPL (C-weighted) via Etymotic ER-2 ear insert drivers. Stimuli are generated by a PC sound card (Creative Audigy 2 Platinum) under the control of a Presentation stimulus delivery program (Neurobehavioural Systems) running under Windows XP. Stimuli are presented as isochronous beats in three conditions: 390ms (condition 1), 585ms (condition 2) and 780ms (condition 3), in blocks of 350 repetitions with each block being presented twice for a total of 700 repetitions of each condition. One of the two blocks which had less amount of artifact is chosen for subsequent analysis. Blocks are presented in one of 4 different random orders to each participant. The total experiment

duration is approximately 1h30m including instrumentation of the subject. The electroencephalogram (EEG) is recorded using 128 electrodes with a Biosemi ActiveTwo amplifier. EEG is sampled at 2048Hz low pass filtered at 417Hz. The electrode array is digitized for each participant (Polhemus Fastrak). EEG is stored as continuous data referenced to the vertex electrode converted offline to average reference.

EEG responses to each stimulus are epoched -300ms to $+600\text{ms}$ using BESA software (version 5.3, MEGIS Software GmbH, Grfelfing, Germany), and epochs including large artifacts ($> 120\mu\text{v}$) are rejected from analysis, leaving 181 ± 14 , 169 ± 35 , and 129 ± 9 (MEAN \pm STD) accepted epochs for conditions 1, 2, and 3, respectively. Epoched data is then exported to Matlab for further analysis. To start analysis, filtering should be applied in the frequency band of interest, where lower beta frequency from 14Hz to 20Hz is chosen. Lower beta frequency has been demonstrated to underlie the neural mechanism in coordination and timing of responses to repetitive tones [12]. The same head model is built as used in the simulations and BEM method is implemented. To perform spatial filtering, covariance matrix is calculated over the whole data and the regularization constant is fixed at 0.01 of the largest eigenvalue of covariance matrix. After source signals of different brain regions have been extracted, we compute appropriate statistical features and further source analysis steps are taken as described in the next sections.

4.2.2 Power Analysis

In this section, we study dynamics of power of cerebral sources obtained from evoked responses in lower beta frequency. Figure 4.9 shows the temporal pattern of the first principal temporal pattern of power given by Eq.3.23. The first principal component

explains 62 ± 12 (MEAN \pm STD) percent of the temporal power signal over all subjects and conditions. As it is obvious, the phase-locked beta power increases after stimuli with maximum around 100ms and follows a decrease between 200 and 300ms. The peak of power around 100ms is expected, as it corresponds to the time when N1 peak occurs. The time corresponding to decrease of beta power is close to the previous finding with MEG [12], where event-related power (results from time-locked activity) desynchronized at all conditions around 200ms. Figure 4.10 shows the source distribution computed by Eq.3.24 corresponding to the first principal temporal power pattern, which is averaged over three subjects (since a general view of sources is of interest in this research) and normalized to be within the the same range from 0 to 1. Visually, the left auditory cortex can be identified in the three conditions as the active brain region, stronger than the right auditory source. The local maxima in the auditory region is identified among the vertices having the same anatomical label based on their talairach coordinates. Statistical t test is applied to the identified source across all conditions and subjects. Its activity is found to be significant ($p < 0.001$). (p denotes p-value which is defined as the probability of obtaining a test statistic as extreme as possible, given null hypothesis is true.) In the next section, this source in the left auditory region is defined as the reference in the analysis of cortico-cortical coherence.

4.2.3 Coherence based Network

The instantaneous coherence is calculated between the reference source identified in the phase-locked response and all the other sources by the two coherence metrics MSC and IC. The temporal coherence values forms the data matrix and the first

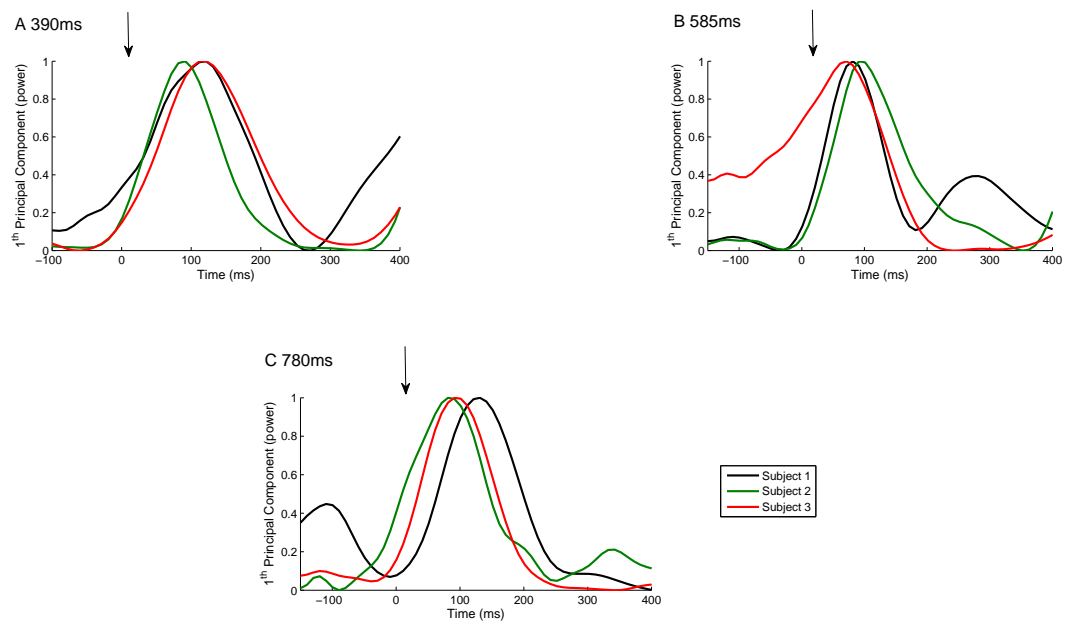


Figure 4.9: The temporal pattern of the first principal component of power fluctuations obtained from the phase-locked activity of brain sources. Overlaid power patterns of three subjects in A:390ms , B:585ms, and C:780ms conditions.

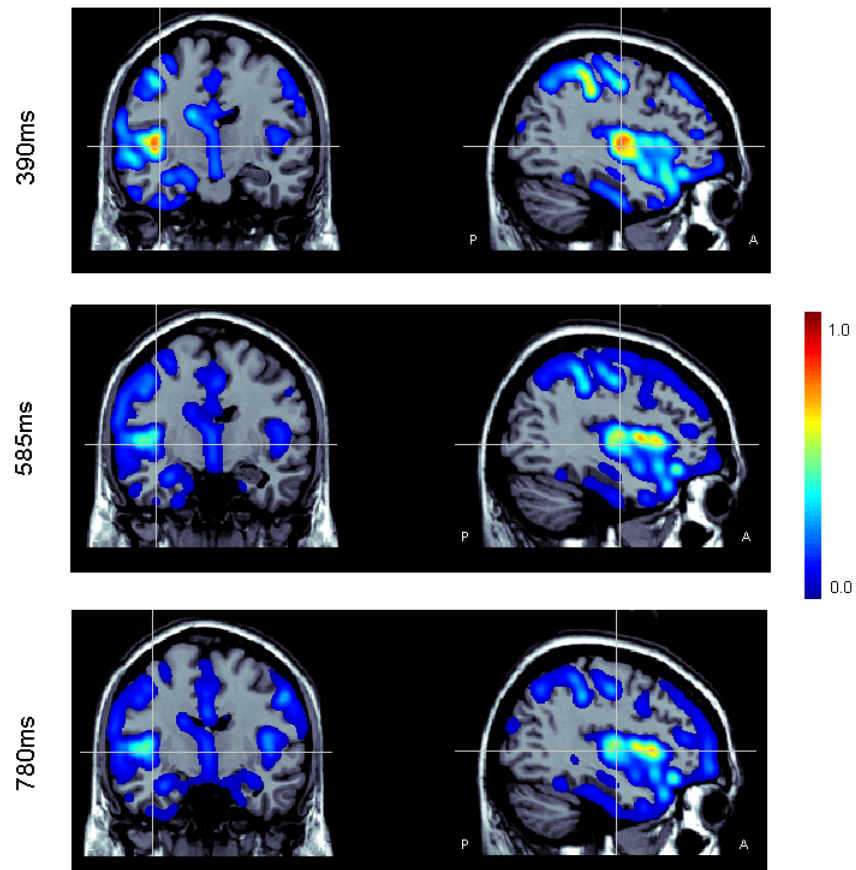


Figure 4.10: The source distribution corresponding to temporal patterns shown in Fig.4.9, averaged over subjects and projected onto the standard brain (sagittal and coronal views). Results are normalized and shown for the three conditions.

principal component and the corresponding source distribution are calculated using Eq.3.23 and Eq.3.24 in Chapter 3. The first principal component explains 62 ± 12 (MEAN \pm STD) percent for the combined two coherence measures over conditions and subjects, in this experiment. The first principal component of the three individual subjects for the three conditions are shown in Figure 4.11. The figure shows the main dynamic changes in coherence among brain sources based on the two coherence measures. Right column corresponding to MSC and left column corresponding to IC show following results.

A peak of coherence reduction occurs just after stimuli for conditions 390ms and 580ms. This peak occurs around the same time in 390ms for three subjects but with some shifts for condition 580ms. The maximum peak after stimuli occurs for 390ms condition around 300ms for three subjects. But, in 580ms condition, the maximum peak occurs at different shifts 100 to 350ms for three subjects. In 780ms condition, the coherence waveform is different from the other two conditions, the maximum peak occurs around the time of stimuli $[-100,100\text{ms}]$ consistent for three subjects.

A peak of coherence reduction is not clearly observable around the time of stimuli by IC measure, as can be seen by MSC, except for a few subjects in conditions 390ms and 585ms. However, a peak of increase in coherence is consistently seen for three subjects in both conditions between 100 and 300ms. This maximum peak almost coincides with the results of MSC. In condition 780ms, except for one subject, the local maximum peak after stimuli is observable around the same time as the other two conditions. Furthermore, in this condition, the maxima around the time of stimuli are consistent with finding by MSC. The coherence decrease after 250ms is obvious for all conditions and subjects by IC measure, comparable to the results of MSC (in

which this reduction occurs after 300ms).

We can conclude several points by comparing the two coherence measures. The coherence increase around the time of stimuli is mainly due to zero phase-locking, since it is absent when IC measure is used instead of MSC. Zero phase-locking may be caused by spatial filtering or the original activity of sources. This is not clear yet. But, if the former is true, IC can eliminate it considerably. In contrast, the peak of coherence after stimuli is mainly due to nonzero phase-locked coherency of neural sources, as it is elaborated by both of coherence measures. The consistency of reduction in two coherence measures after 300ms also emphasizes the suppression of nonzero phase-locking behavior of sources in response to stimuli.

Figure 4.12 illustrates the source distribution corresponding to the first principal coherence pattern which belongs to one of the subjects in three different conditions. This figure is top view of cerebral cortex obtained from the standard MRI. The top row shows the results of MSC and illustrate several regions dynamically coherent with the left auditory source. The below row is the source distribution obtained by IC metric, a scattered distribution around the sensorimotor area³ is observable. All figures are normalized to be within the same range [0,1] for illustration purpose. An average of absolute value of source distribution over conditions and subjects is computed and local maxima are detected. The average is projected on the cerebral cortex and is displayed in Figure 4.13. Statistical t test is applied to find the significant local maxima whose average is significantly greater than zero. A list of anatomical labels based on talairach coordinates [22], resulted from each measure is described in Table 4.1. Comparing the two source distributions from two coherence metrics can result in

³A region of cerebral cortex, located around central sulcus and performs sensorimotor-related functions. Central sulcus separates parietal lobe from frontal lobe.

Coherence metric	Anatomical labels	p-value	
MSC	Superior temporal gyrus (R)	0.0002	
	Superior parietal lobule (LR)	0.0001	
	Inferior parietal lobule (L)	< 0.0001	
	Precentral, postcentral gyrus (R)	< 0.0001	
	Precuneus (LR)	< 0.0001	
	Superior frontal gyrus (L)	< 0.0001	
	Superior, inferior temporal gyrus (L)	< 0.0001	
	Precentral gyrus (L)	< 0.0001	
	Parahippocampal gyrus (R)	< 0.0001	
	Fusiform gyrus (LR)	< 0.0001	
	Middle frontal gyrus (LR)	< 0.0001	
	IC	Middle temporal gyrus (L)	0.0008
		Middle temporal gyrus (L)	0.0008
Precentral gyrus (L)		0.0002	
Superior, inferior temporal gyrus (L)		0.0001	

Table 4.1: Anatomical labels of significant sources found by the first principal component (significance level (α)=0.001). The test is performed over conditions and subjects. L refers to left, R refers to right, and LR refers to both left and right.

following observations. The right sensorimotor area is common in the results of two coherence metrics, as table information and highest intensity in Figure 4.13 (shown by the red color) indicate. This is in accordance with the previous findings [6],[12],[15], and [32], regarding recruitment of motor region in repetitive tone perception. The other regions found by MSC indicated in Table 4.1 are also consistent with recent MEG results [12], which used MSC. These regions include superior, inferior temporal gyrus (L), and precentral gyrus (L) found to be coherent with left auditory source. Other anatomical regions found by MSC in our research can also be found in other related networks in auditory rhythm perception detected in [12].

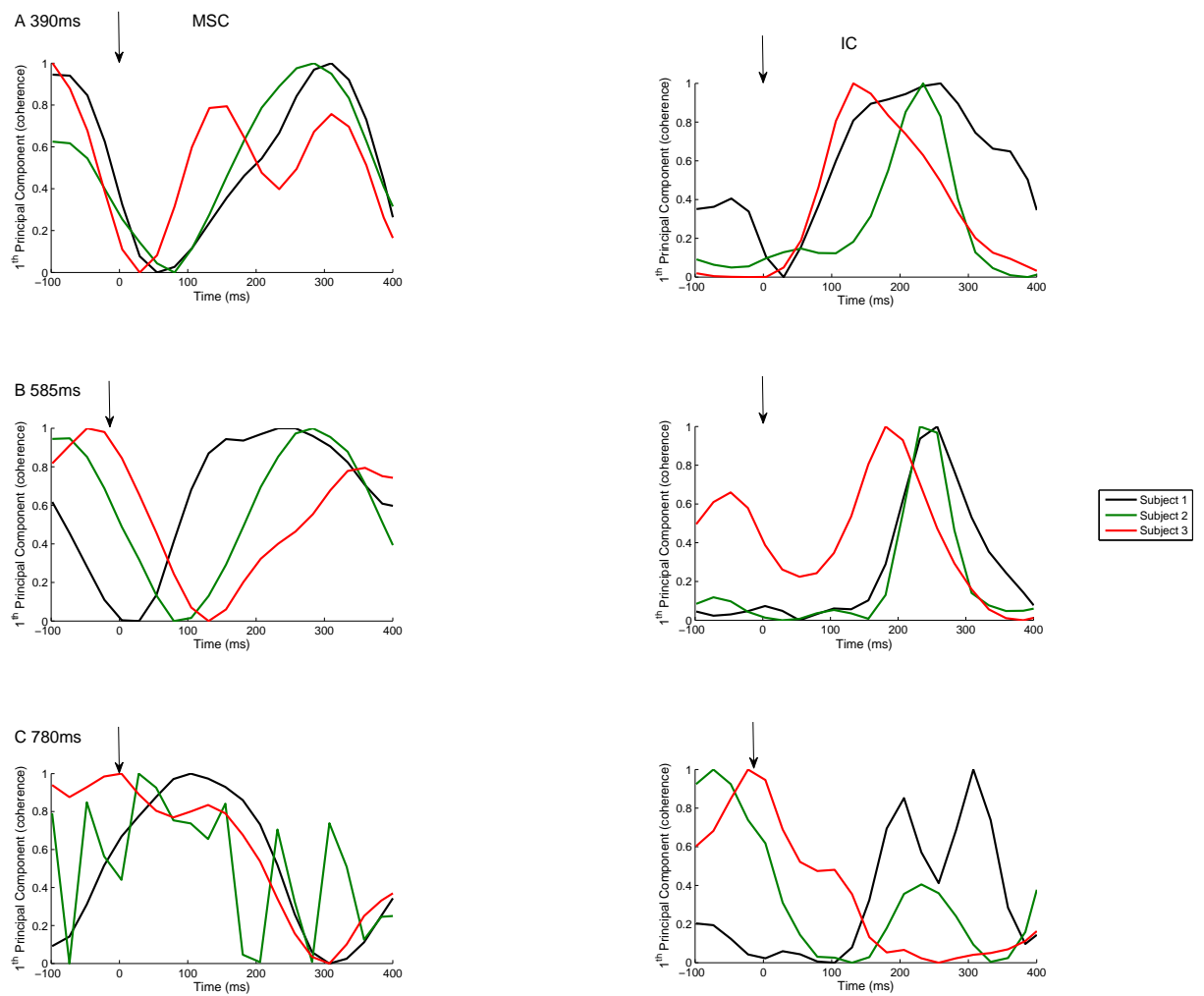


Figure 4.11: The first principal temporal coherence with left auditory source, shown for three individual subjects for A:390ms , B:585ms, and C:780ms conditions. Right column contains IC results and Left column contains MSC results.

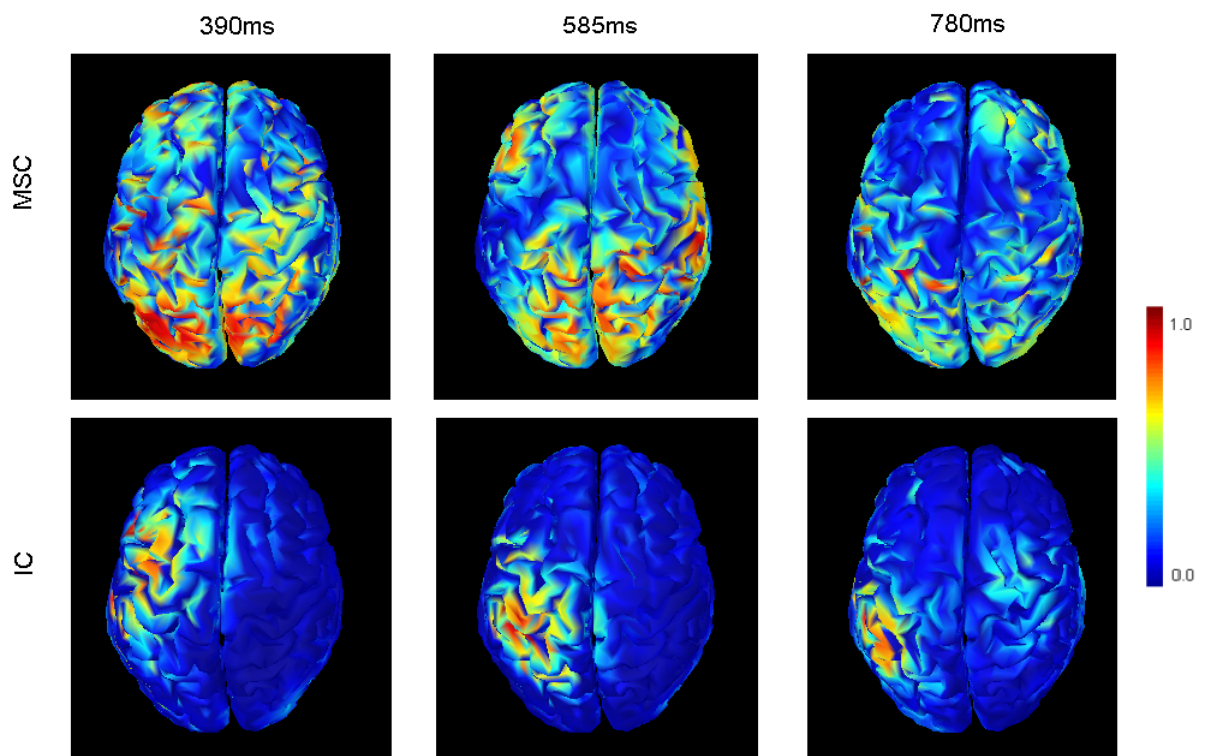


Figure 4.12: Source distribution corresponding to the first principal component normalized to be in the range from 0 to 1 as shown in a color bar. Source distribution belongs to one of the subjects.

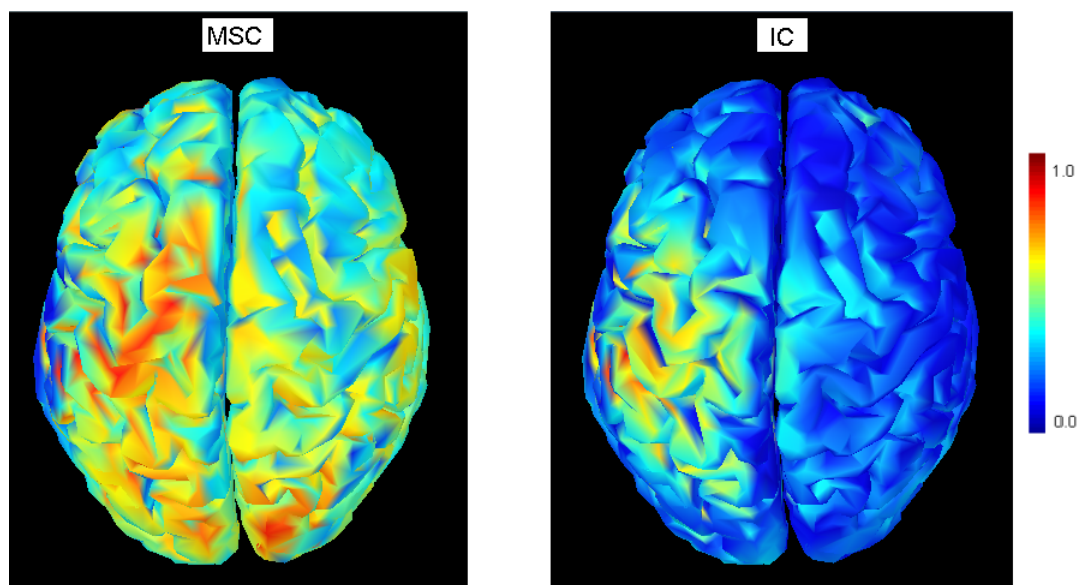


Figure 4.13: Normalized average of source distribution (absolute values) corresponding to the first principal component. The average is made over all subjects and conditions.

Chapter 5

Summary, Future Work, and Conclusion

5.1 Summary and Conclusion of Thesis

This study provided a framework to study dynamics of power and coherence based on EEG signals as follows. We applied spatial filtering to estimate neural time series of brain, given scalp EEG signals. This was to avoid volume conduction effect in the interpretation of neural source behavior if studied directly by scalp measurements. Instantaneous power (power analysis) and coherence (coherence analysis) were subsequently calculated and dynamics of population's neural responses was analyzed with singular value decomposition. In the coherence analysis, we used imaginary component (IC) besides the conventional measure magnitude-squared coherence (MSC) to suppress cross-talk of spatial filtering solution.

It was shown mathematically and with computer simulations that the elimination of mean from MSC cannot completely avoid the cross-talk problem in the low SNR

situation. Further, in the simulations, power analysis results showed the ability of the explained method to localize sources whose power is periodically changing with stimuli. It could localize them in their true locations and also identify the true corresponding power pattern. In addition, we discussed the effect of regularization of the spatial filtering on the coherence results and showed that regularization constant may distort the coherence waveform if chosen to be very low proportion of the highest eigenvalue of covariance matrix in the low SNR situation. Higher amount of regularization generally ensures higher amount of output SNR thereby implicitly leading to a more reliable coherence representation, but the lower spatial resolution of the corresponding output source image is the cost of it. This fact was confirmed and clarified with the simulations.

Then, we applied the procedure to real EEG recordings made from three subjects who were listening to repetitive auditory stimuli in three different but close rates. The EEG data were filtered from 14 Hz to 20 Hz (beta1 band), as shown in previous studies [12],[32] to understand neural mechanism in response to these stimuli. We took into account our simulation findings with regard to the regularization constant; we used higher amount of regularization in the real data to make sure that we obtained output signal-to-noise-ratio as high as possible. The study of the real data was performed in the aspect of phase-locked power and coherence. In the power analysis, power of the evoked response was calculated and in coherence analysis, coherence based on the two measures IC and MSC was calculated on the trial basis. The source of left auditory cortex was detected by the power analysis and had the maximum power in all subjects and conditions approximately 100ms after stimuli (the same time as N1 peak usually occurs). Then, it was considered as the reference in coherence analysis.

The IC and MSC results were compared in terms of the first principal coherence waveform and their corresponding source image with respect to the reference source. Also, the results of previous finding in the role of motor regions to coordinate with auditory cortex in the perception of rhythmic auditory tones were presented and were shown to be comparable with our results. The sources detected in the real data were also found in other studies with fMRI and MEG [12],[6],[15], and [32], which explored the sources underlying auditory rhythm perception.

5.1.1 Main Aspects of Research and Future Work

This study can be considered as a part of a big step to spatially and temporally localize with high resolution brain sources functionally recruited to perceive any stimuli trains causing dynamic changes in brain. We mainly focused on the effect of rhythmic auditory stimuli on brain and how neural sources process these stimuli. It was shown that EEG signals can be used to track neural responses dynamically co-changing in power and in coherence. The advantage of using EEGs is that they have a superior temporal resolution to fMRI and on the other hand they are more available and economical than MEGs.

In this study, the source in the auditory cortex was correctly identified in the power analysis of evoked response in beta1 frequency band, where the source is consistent with the previous studies on the neural sources of the evoked response components [33], [19]. The results also confirm the previous finding with MEG and fMRI regarding the involvement of sensorimotor area in the perception of the auditory stimuli trains and its coherency with the auditory source. This research shows the superiority of IC to MSC coherence metric in terms of canceling zero-phase locked coherency which

is mainly due to spatial filtering. However, the reason for the inconsistency of IC and MSC over time with respect to stimuli needs to be more clarified. This may be possible by applying IC to MEG signals or employing direct measurements of cerebral cortex and compare them with the EEG results. The reason for individual differences in the coherence waveforms and the associated differences in their anatomical regions need be studied in more details. Therefore, a higher number of subjects needs to be experimented in order to see if their anatomical regions of activity have any correlation with the individual differences in the coherence waveforms. Finally, improving accuracy of forward model, for instance considering the anisotropic properties of brain tissues and using individual head geometries instead of a standard MRI, may have a considerable improvement on the inverse solutions and thereby power and coherence results.

Bibliography

- [1] Barth, D. and Di, S. (1990). Three-dimensional analysis of auditory-evoked potentials in rat neocortex. *Journal of neurophysiology*, **64**(5), 1527–1536.
- [2] Bendat, J. and Piersol, A. (2011). *Random data: analysis and measurement procedures*, volume 729. Wiley.
- [3] Brebbia, C., Telles, J., and Wrobel, L. (1984). Boundary element techniques: theory and applications in engineering. *Berlin and New York, Springer-Verlag, 1984, 478 p.*
- [4] Bruns, A. (2004). Fourier-, hilbert-and wavelet-based signal analysis: are they really different approaches? *Journal of neuroscience methods*, **137**(2), 321–332.
- [5] Cai, Y., Lou, W., Li, M., and Li, X.-Y. (2007). Target-oriented scheduling in directional sensor networks. In *INFOCOM 2007. 26th IEEE International Conference on Computer Communications. IEEE*, pages 1550 –1558.
- [6] Chen, J., Penhune, V., and Zatorre, R. (2008). Listening to musical rhythms recruits motor regions of the brain. *Cerebral Cortex*, **18**(12), 2844–2854.
- [7] Dalal, S., Guggisberg, A., Edwards, E., Sekihara, K., Findlay, A., Canolty, R., Berger, M., Knight, R., Barbaro, N., Kirsch, H., *et al.* (2008). Five-dimensional

- neuroimaging: localization of the time–frequency dynamics of cortical activity. *Neuroimage*, **40**(4), 1686–1700.
- [8] Dale, A. and Sereno, M. (1993). Improved localization of cortical activity by combining eeg and meg with mri cortical surface reconstruction: A linear approach. *Journal of Cognitive Neuroscience*, **5**(2), 162–176.
- [9] Dale, A., Liu, A., Fischl, B., Buckner, R., Belliveau, J., Lewine, J., and Halgren, E. (2000). Dynamic statistical parametric neurotechnique mapping: combining fmri and meg for high-resolution imaging of cortical activity. *Neuron*, **26**(1), 55–67.
- [10] Dossevi, A., Cosmelli, D., Garnero, L., and Ammari, H. (2008). Multivariate reconstruction of functional networks from cortical sources dynamics in meg/eeg. *Biomedical Engineering, IEEE Transactions on*, **55**(8), 2074–2086.
- [11] Fuchs, A. (2007). Beamforming and its applications to brain connectivity. *Handbook of Brain Connectivity*, pages 357–378.
- [12] Fujioka, T., Trainor, L., Large, E., and Ross, B. (2012). Internalized timing of isochronous sounds is represented in neuromagnetic beta oscillations. *The Journal of Neuroscience*, **32**(5), 1791–1802.
- [13] Gerloff, C., Richard, J., Hadley, J., Schulman, A., Honda, M., and Hallett, M. (1998). Functional coupling and regional activation of human cortical motor areas during simple, internally paced and externally paced finger movements. *Brain*, **121**(8), 1513–1531.
- [14] Godey, B., Schwartz, D., De Graaf, J., Chauvel, P., and Liegeois-Chauvel, C.

- (2001). Neuromagnetic source localization of auditory evoked fields and intracerebral evoked potentials: a comparison of data in the same patients. *Clinical neurophysiology*, **112**(10), 1850–1859.
- [15] Grahn, J. and Brett, M. (2007). Rhythm and beat perception in motor areas of the brain. *Journal of Cognitive Neuroscience*, **19**(5), 893–906.
- [16] Gramfort, A., Papadopoulos, T., Olivi, E., Clerc, M., *et al.* (2010). Openmeeg: opensource software for quasistatic bioelectromagnetics. *Biomedical engineering online*, **9**(1), 45.
- [17] Guggisberg, A., Dalal, S., Zumer, J., Wong, D., Dubovik, S., Michel, C., and Schnider, A. (2011). Localization of cortico-peripheral coherence with electroencephalography. *Neuroimage*, **57**(4), 1348–1357.
- [18] He, B., Yao, D., Lian, J., and Wu, D. (2002). An equivalent current source model and laplacian weighted minimum norm current estimates of brain electrical activity. *Biomedical Engineering, IEEE Transactions on*, **49**(4), 277–288.
- [19] Herdman, A., Wollbrink, A., Chau, W., Ishii, R., Ross, B., and Pantev, C. (2003). Determination of activation areas in the human auditory cortex by means of synthetic aperture magnetometry. *Neuroimage*, **20**(2), 995–1005.
- [20] Hipp, J., Engel, A., and Siegel, M. (2011). Oscillatory synchronization in large-scale cortical networks predicts perception. *Neuron*, **69**(2), 387.
- [21] Hui, H., Pantazis, D., Bressler, S., and Leahy, R. (2010). Identifying true cortical interactions in meg using the nulling beamformer. *NeuroImage*, **49**(4), 3161–3174.

- [22] Lancaster, J., Woldorff, M., Parsons, L., Liotti, M., Freitas, C., Rainey, L., Kochunov, P., Nickerson, D., Mikiten, S., and Fox, P. (2000). Automated talairach atlas labels for functional brain mapping. *Human brain mapping*, **10**(3), 120–131.
- [23] Leocani, L., Toro, C., Manganotti, P., Zhuang, P., and Hallett, M. (1997). Event-related coherence and event-related desynchronization/synchronization in the 10 hz and 20 hz eeg during self-paced movements. *Electroencephalography and Clinical Neurophysiology/Evoked Potentials Section*, **104**(3), 199–206.
- [24] Mitzdorf, U. (1987). Properties of the evoked potential generators: current source-density analysis of visually evoked potentials in the cat cortex. *International Journal of Neuroscience*, **33**(1-2), 33–59.
- [25] Mosher, J., Leahy, R., and Lewis, P. (1999). Eeg and meg: forward solutions for inverse methods. *Biomedical Engineering, IEEE Transactions on*, **46**(3), 245–259.
- [26] Nolte, G., Bai, O., Wheaton, L., Mari, Z., Vorbach, S., Hallett, M., *et al.* (2004). Identifying true brain interaction from eeg data using the imaginary part of coherency. *Clinical Neurophysiology*, **115**(10), 2292–2307.
- [27] Nunez, P. and Srinivasan, R. (2005). *Electric fields of the brain: the neurophysics of EEG*. Oxford University Press, USA.
- [28] Ord, K. (1996). Outliers in statistical data : V. barnett and t. lewis, 1994, 3rd edition, (john wiley & sons, chichester), 584 pp., [uk pound]55.00, isbn 0-471-93094-6. *International Journal of Forecasting*, **12**(1), 175–176.

- [29] Pascual-Marqui, R. *et al.* (2002). Standardized low-resolution brain electromagnetic tomography (sloreta): technical details. *Methods Find Exp Clin Pharmacol*, **24**(Suppl D), 5–12.
- [30] Pascual-Marqui, R., Biscay, R., Valdes-Sosa, P., Bosch-Bayard, J., and Riera-Diaz, J. (2011). Cortical current source connectivity by means of partial coherence fields. *arXiv preprint arXiv:1108.0251*.
- [31] Pfurtscheller, G. and Lopes da Silva, F. (1999). Event-related eeg/meg synchronization and desynchronization: basic principles. *Clinical neurophysiology*, **110**(11), 1842–1857.
- [32] Pollok, B., Südmeyer, M., Gross, J., and Schnitzler, A. (2005). The oscillatory network of simple repetitive bimanual movements. *Cognitive brain research*, **25**(1), 300–311.
- [33] Scherg, M. and Berg, P. (1991). Use of prior knowledge in brain electromagnetic source analysis. *Brain Topography*, **4**(2), 143–150.
- [34] Sekihara, K. and Nagarajan, S. (2008). *Adaptive Spatial Filters for Electromagnetic Brain Imaging*. Series in Biomedical Engineering. Springer.
- [35] Sekihara, K., Nagarajan, S., Poeppel, D., and Marantz, A. (2002). Performance of an meg adaptive-beamformer technique in the presence of correlated neural activities: effects on signal intensity and time-course estimates. *Biomedical Engineering, IEEE Transactions on*, **49**(12), 1534–1546.
- [36] Sekihara, K., Nagarajan, S., Poeppel, D., and Marantz, A. (2004). Asymptotic snr of scalar and vector minimum-variance beamformers for neuromagnetic source

- reconstruction. *Biomedical Engineering, IEEE Transactions on*, **51**(10), 1726–1734.
- [37] Sekihara, K., Sahani, M., and Nagarajan, S. (2005). Localization bias and spatial resolution of adaptive and non-adaptive spatial filters for meg source reconstruction. *Neuroimage*, **25**(4), 1056–1067.
- [38] Sekihara, K., Owen, J., Trisno, S., and Nagarajan, S. (2011). Removal of spurious coherence in meg source-space coherence analysis. *Biomedical Engineering, IEEE Transactions on*, **58**(11), 3121–3129.
- [39] Snyder, J. and Large, E. (2005). Gamma-band activity reflects the metric structure of rhythmic tone sequences. *Cognitive Brain Research*, **24**(1), 117–126.
- [40] Srinivasan, R., Winter, W., Ding, J., and Nunez, P. (2007). Eeg and meg coherence: measures of functional connectivity at distinct spatial scales of neocortical dynamics. *Journal of neuroscience methods*, **166**(1), 41–52.
- [41] Strang, G. and Fix, G. (2008). *An Analysis of the Finite Element Method*, 2ed. Wellesley-Cambridge Press.
- [42] Tadel, F., Baillet, S., Mosher, J., Pantazis, D., and Leahy, R. (2011). Brainstorm: a user-friendly application for meg/eeg analysis. *Computational intelligence and neuroscience*, **2011**, 8.
- [43] Talairach, J. and Tournoux, P. (1988). *Co-planar stereotaxic atlas of the human brain*, volume 147. Thieme New York:.
- [44] Toma, K., Mima, T., Matsuoka, T., Gerloff, C., Ohnishi, T., Koshy, B., Andres,

- F., and Hallett, M. (2002). Movement rate effect on activation and functional coupling of motor cortical areas. *Journal of neurophysiology*, **88**(6), 3377–3385.
- [45] Van Veen, B., Van Drongelen, W., Yuchtman, M., and Suzuki, A. (1997). Localization of brain electrical activity via linearly constrained minimum variance spatial filtering. *Biomedical Engineering, IEEE Transactions on*, **44**(9), 867–880.
- [46] Woolrich, M., Hunt, L., Groves, A., and Barnes, G. (2011). Meg beamforming using bayesian pca for adaptive data covariance matrix regularization. *NeuroImage*, **57**(4), 1466–1479.